Theoretical and experimental free vibration analysis of a beam-tendon system with an eccentrically placed tendon

V. Ondra[a,*], B. Titurus[a]

[a] *University of Bristol, Department of Aerospace Engineering, University Walk, BS8 1TR Bristol, United Kingdom*

Abstract

Theoretical and experimental free vibration analysis of a beam-tendon system is presented in this paper. The system consists of a thin-walled cantilever beam with an open cross-section and a tip mass which is loaded by an eccentrically placed tendon. The novel beam-tendon system is modelled using a set of partial differential equations and numerical free vibration analysis is conducted using a boundary problem solver. The results are thoroughly validated using a bench-top experiment and a high-fidelity finite element model. The effect of the tendon location on the frequency-loading diagrams is systematically investigated for the first time. The results demonstrate that the location of the tendon significantly influences natural frequency shifts caused by the applied axial load and it is observed that some natural frequencies can even increase with the increasing compressive axial loading for certain locations of the tendon. In addition, veering between the beam-dominated and tendon-dominated modes is studied and the structural stability of the system is discussed. The paper concludes with suggestions of practical applications of a beam-tendon system with an eccentrically placed tendon.

Keywords: beam-tendon system, free vibration analysis, eccentric axial loading, frequency loci veering, frequency-loading diagram

Highlights

- A beam axially loaded by an eccentrically placed tendon is studied
- A theoretical model of the beam-tendon system is validated using an FE model and experimentally
- The effect of tendon location is shown to have significant effect on modal properties
- Frequency loci veering between beam-dominated and tendon-dominated modes is observed
- The impact of the tendon location on the structural stability is discussed

Nomenclature

Symbol	Description
A	Area of the cross-section, m^2
e_y, e_z	Coordinates of the tendon location, m
E	Young's modulus of elasticity, Pa
f	Natural frequency, Hz
G	Shear modulus of elasticity, Pa

*Corresponding author.
Email addresses: vaclav.ondra@bristol.ac.uk (V. Ondra), brano.titurus@bristol.ac.uk (B. Titurus)

I_{tip}	Mass moment of inertia of the tip fixture, kg m^2
I_y, I_z	Sectional moments of inertia of the cross-section about y and z axis, m^4
J	Torsional constant, m^4
L	Total length of the beam and tendon, m
L_y, L_z	External excitation forces in y and z directions, N
m	Mass of the beam per unit length, kg m^{-1}
m_{t}	Mass of the tendon per unit length, kg m^{-1}
M_{tip}	Tip mass, kg
N_m	Number of considered modes
P	Applied axial force, N
P_{cr}	Critical force, N
Q	External excitation moment about elastic axis (torque), N m
r_c	Polar radius of gyration about mass axis, m
t	Time, s
v, w	Bending displacements of beam in y and z directions, m
v_{t}, w_{t}	Transversal displacements of tendon in y and z directions, m
$W, W_{\text{t}}, V, V_{\text{t}}, \Phi$	Mode shape components of the beam-tendon system
$\overline{W}, \overline{V}$	Mode shapes evaluated in the place of experimental measurement
x	Independent spatial variable, m
y, z	Coordinate axes in the plane of the cross-section
y_a, z_a	Coordinates of the experimental measurements, m
y_0	Distance between the mass and elastic axes, m
β_y	Cross-sectional parameter, m
Γ	Warping moment of inertia, m^6
ϕ	Torsional displacement, rad
ω	Angular frequency, rad s^{-1}
Ψ	Mode shape of the system
$\dot{(\bullet)}$	Partial derivative with respect to time
$(\bullet)'$	Partial derivative with respect to spatial variable
ABQ	Marks results obtained using Abaqus
BC	Boundary condition
BM	Marks results obtained from beam model without warping
BMW	Marks results obtained from beam model with warping
c.g.	Centre of gravity
EoM	Equations of motion
FRF	Frequency response function
MAC	Modal assurance criteria
LSCF	Least-square complex frequency estimator
F-L	Frequency-loading
ODE	Ordinary differential equation
PDE	Partial differential equation
s.c.	Shear centre

1. Introduction

In this paper, a thin-walled beam with an open mono-symmetric cross-section which is subjected to the axial loading generated by an eccentrically placed tendon is investigated. Dynamics of beams and tendons (taut strings, cables) has been previously extensively studied, due to their frequent usage in engineering applications. The beams mostly present the main structural elements while tendons are often utilised as actuators or a means of vibration control as reviewed in [1, 2]. An overwhelming number of studies that focus on different aspects of beam and string modelling, application and testing has been published [3–6].

A number of studies also investigated vibration of axially loaded beams [7] and their stability [8, 9]. It was often assumed that the axial force acts through the centroid of an open cross-section. For example, in [10] dynamic stiffness matrix for an axially loaded beam element was derived. Similarly, beam element matrices based on Vlasov's theory of axially loaded beam were derived in [11, 12]. In [13] bending and torsional vibration of thin-walled Euler-Bernoulli beam loaded through the centroid was presented. It has been also acknowledged that, despite not being extensively studied, the eccentric axial loading can significantly influence the structural stability of thin-walled beams [14]. The equations of motion describing the stability of eccentrically loaded thin-walled beams were derived in [9, 15], and further augmented by an effect of warping and axial displacement in [8].

In the previous studies, the effect of the axial loading on the structural stability and vibration has been investigated, but it was not considered how such an axial force is applied. In contrast, the axial force was induced by tendons, for example, in [16] where large-deflection equilibrium and small vibrations about this equilibrium were considered, or in [17, 18] where the use of the axial load for control of vibration response was examined. Tendons have also been used to support beams during experimental studies as shown in [19]. However, none of the previous papers considered the tendon response and its effect on dynamics of the system. On the other hand, a coupled system which consists of a cantilever beam which is axially loaded by a tendon is considered in this paper. The tendon is attached at the tip of the beam, freely passes through its body parallel to the elastic axis, and is fixed and loaded in the same plane as the beam. Since the motions of the beam and the tendon influence each other, they create a coupled beam-tendon system, and the beam and the tendon must be modelled and analysed simultaneously.

A simple beam-tendon system was previously investigated in [20, 21] both numerically and experimentally. It was found that the beam-tendon system exhibits reduction in the beam's natural frequencies due to the tendon-induced axial force as well as veering between beam-dominated and tendon-dominated modes. These findings were further numerically examined in [22] for rotating pre-twisted beams and for a system with intermittently attached tendon in [23, 24]. It was shown that although the rotation has a considerable effect on the tendon, the tendon is still able to influence the modal characteristics of the beam significantly. Therefore, it has been suggested to incorporate a tendon in a rotorcraft blade to introduce a means of controlling its dynamics properties [25]. This was shown [26] as a possible resonance avoidance mechanism which allows rotorcraft to operate with shape adaptive blades or with variable rotor speed, thereby increasing their performance and efficiency. In all these studies, the tendon was attached to the beam's tip so that the place of the attachment coincided with the shear centre of the beam. Moreover, in the experimental studies [20, 21, 24] a cantilever beam with a double symmetry cross-section has been used so the elastic and mass axis were the same. A mono-symmetric channel cross-section was however also experimentally studied in [27], but the effect of the tendon placement has not been systemically investigated. To the best knowledge of the authors, the beam-tendon system, consisting of a mono-symmetric open cross-section beam and an eccentrically placed tendon, which is presented in this paper has not been previously studied.

The paper is organised as follows: the theoretical model of the system, given by a set of partial differential equations and boundary conditions, is introduced in section 2, where the numerical procedure used to obtain the modal properties and a finite element model of the system are also described. The results of the numerical free vibration analysis are then experimentally validated in section 3 for three selected locations of the tendon (in the elastic axis, in the mass axis and in a general location). In section 4 further investigations of the effect of the tendon location are conducted. Firstly, the effect of the tendon location on the natural frequencies of the system is investigated both experimentally and computationally using the validated theoretical model. Then, the effect of the tendon location on structural stability is discussed. In section 5 the main findings of the study are summarised, the limitations and assumptions of the theoretical model are discussed and possible applications of the beam-tendon system with an eccentrically placed tendon are suggested.

2. Theoretical model

The system under consideration is an isotropic straight thin-walled cantilever beam with mono-symmetric cross-section loaded by an eccentrically placed tendon as depicted in Fig. 1. The eccentrically placed tendon is attached at the tip of the beam, passes through its whole body parallel to the elastic axis, and is fixed

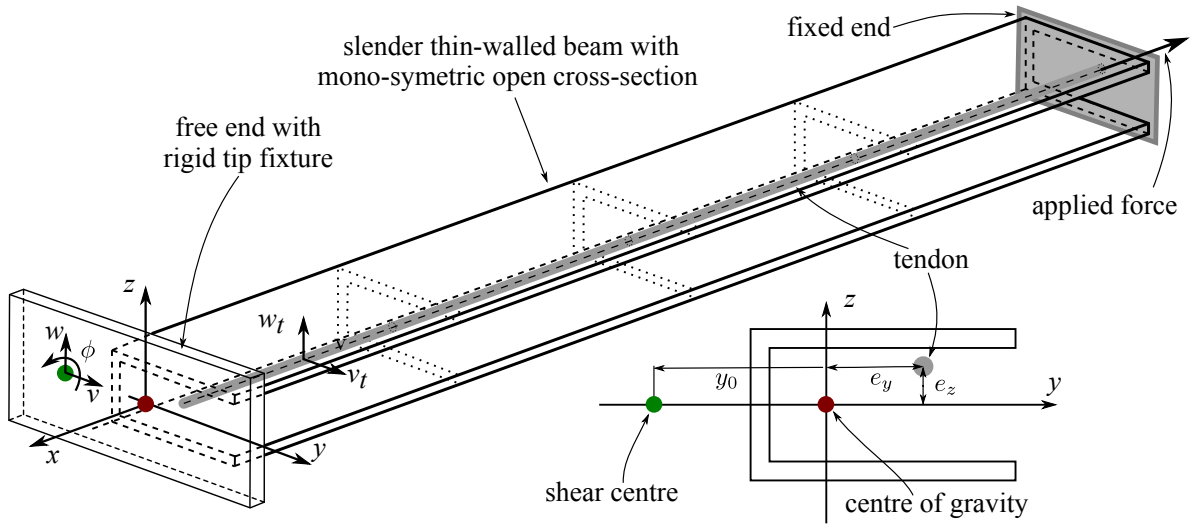

Figure 1: The beam-tendon system studied: it consists of an isotropic thin-walled cantilever beam which features an offset between the mass and elastic axes, and which is subjected to an eccentric tendon-induced axial load. The tendon is connected to the tip of the beam, passes freely through its whole body parallel to the elastic axis and is fixed and loaded in the same plane as the beam.

and loaded in the same plane as the beam. Unlike in the previous studies [21, 22, 26, 27], the tendon does not coincide with the elastic or mass axis and can be placed in any point of the cross-section as long as it does not collide with the walls of the beam during its motion. The tendon is attached using a tip fixture, characterised by its mass and moment of inertia. The tip fixture is assumed to be perfectly rigid and allows the tendon to be placed even outside the beam's cross-section. The motion of the beam is described by flapping (out-of-plane, vertical bending in the z direction) displacement of the elastic axis, lead-lag (in-plane, horizontal bending in the y direction) displacement of the elastic axis, and torsion of the cross-section about the elastic axis. The out-of-plane bending and torsion motions are mutually coupled through the cross-sectional offset of the elastic and mass axes. The parameters characterising the beam are uniformly distributed, i.e. they do not vary along the span of the beam. It is assumed that the beam meets all the requirement of the Euler-Bernoulli theory and can therefore be modelled by the linear Euler-Bernoulli theory with warping [8, 9] which accounts for the tendon-induced axial loading. It is further assumed that the static bending deflection caused by an eccentrical placement of the tendon is small and can be neglected. The tendon is modelled using the wave equations and it is assumed that it does not change its cross-sectional area under loading [6]. Both the beam and the tendon are fixed (clamped) at one end and coupled with each other through the geometrical and loading boundary conditions at the other end. At the tip, their displacements are identical and the tendon-induced axial force contributes to the shear and moment boundary conditions of the beam. Unlike [23, 24], no other connectivity conditions were enforced since the tendon is free to vibrate inside the beam.

2.1. Equations of motion and boundary conditions

The equations of motion (EoM) describing the coupled beam-tendon system consist of three equations for the motion of the beam, and two equations of the motion of the tendon. The Hamilton's principle can be used to derive the equations of the axially loaded beam as detailed in [8] as well as the wave equations describing the tendon as shown in [3]. The EoM describing the coupled beam-tendon system can be then written as

$$EI_z w'''' + Pw'' - P(y_0 - e_y)\phi'' + m(\ddot{w} - y_0\ddot{\phi}) = L_z, \tag{1a}$$

$$EI_y v'''' + Pv'' - Pe_z\phi'' + m\ddot{v} = L_y, \tag{1b}$$

$$E\Gamma\phi'''' - (GJ - P\beta_y e_y - Pr_c^2)\phi'' - Pe_z v'' - P(y_0 - e_y)w'' + m(r_c^2\ddot{\phi} - y_0\ddot{w}) = Q, \tag{1c}$$

$$-Pw_t'' + m_t\ddot{w}_t = 0, \tag{1d}$$

$$-Pv_t'' + m_t\ddot{v}_t = 0. \tag{1e}$$

where $w(t,x)$, $v(t,x)$ are the flapping and lead-lag bending displacements of the elastic axis of the beam, $v_\mathrm{t}(t,x)$, $w_\mathrm{t}(t,x)$ are the flapping and lead-lag transversal displacements of the tendon, $\phi(t,x)$ is the torsional displacement about the elastic axis, t is time, x is the independent spatial variable measured spanwise from the fixed end of the system, E is Young's modulus of elasticity, G is a shear modulus of elasticity, I_z and I_y are centroidal moments of inertia, J is a torsion constant, Γ is a warping moment of inertia, y_0 is the y coordinate of the elastic axis (negative for the channel beam studied), e_y and e_z are the coordinates of the tendon, r_c^2 is the polar radius of gyration about mass axis, m and m_t are the mass per unit length of the beam and tendon, respectively, P is the applied loading force which corresponds to the axial force acting on the beam, L_y, L_z are the external distributed excitation forces in flapping and lead-lag directions, Q is the external excitation moment about the elastic axis (torque), $(\dot{\bullet})$ and $(\bullet)'$ are partial derivatives with respect to time and spatial variable, respectively, and β_y is a cross-sectional parameter defined [8] as

$$\beta_y = \frac{1}{I_y}\int_A y(y^2+z^2)\,\mathrm{d}A - 2y_0,$$

where y and z are principal centroidal axes, and A is the cross-sectional area.

The novelty of these EoM lies in the consideration of the coupled beam-tendon dynamics and an eccentric placement of the tendon. While the EoM in the present form have not been considered in literature, certain similarities with previous studies can be observed. Equations (1a), (1b) and (1c), describing the flapping, lead-lag and torsion of the beam, respectively, are identical to the EoM used to assess structural stability of a beam with an open mono-symmetric cross-section subjected to eccentric axial loading in [8, 9, 15] (the inertia terms were not considered in these studies). For the axial force applied through the cross-sectional centroid, Eqs. (1a)-(1c) reduce to the EoM used in [10, 11, 13] to perform free vibration analysis. For the axial force applied through the elastic axis, and neglecting the effect of warping and the cross-sectional parameter β_y, Eqs. (1a)-(1c) augmented by the effect of centrifugal forces and beam pre-twist were used in [28, 29] to demonstrate a possibility of using the axial force for resonance avoidance in rotorcraft. The full set of EoM in Eq. (1) (including the wave equations describing the motion of the tendon) was used in [21, 27] with no warping and the tendon placed in the elastic axis to perform free vibration analysis of a simpler beam-tendon system. When augmented by the effect of centrifugal forces and beam pre-twist, and for the tendon placed in the elastic axis, and excluding the effect of warping and ignoring the cross-sectional parameter β_y, Eq. (1) were used in [22, 26] to study a rotating blade-tendon system and its application in rotorcraft with variable rotor speed. There are no studies investigating the effect of the tendon sectional position and the coupled beam-tendon dynamics.

The equations of motion are accompanied by a set of boundary conditions (BCs) which ensures the coupling between the beam and the tendon. The BCs at the fixed end of the system for $x = 0$ are

$$w = w' = v = v' = \phi = \phi' = w_t = v_t = 0. \tag{2}$$

The BCs for the free end (for $x = L$, where L is the length of the system) in which the connection between the beam and the tendon is reflected can be written as

$$-Pw' + P(y_0 - e_y)\phi' - EI_z w''' + M_\mathrm{tip}\ddot{w} + \underline{Pw_t'} = 0, \tag{3a}$$

$$\cancel{Pe_z} + EI_z w'' = 0, \tag{3b}$$

$$-Pv' + Pe_z\phi' - EI_y v''' + M_\mathrm{tip}\ddot{v} + \underline{Pv_t'} = 0, \tag{3c}$$

$$\cancel{Pe_y} + EI_y v'' = 0, \tag{3d}$$

$$-E\Gamma\phi''' + (GJ - Pe_y\beta_y - Pr_c^2)\phi' + P(y_0 - e_y)w' + Pe_z v' + I_\mathrm{tip}\ddot{\phi} \underline{- P(y_0 - e_y)w_t' - Pe_z v_t'} = 0, \tag{3e}$$

$$E\Gamma\phi'' = 0, \tag{3f}$$

$$w_t = w - (y_0 - e_y)\phi, \tag{3g}$$

$$v_t = v - e_z\phi. \tag{3h}$$

where M_{tip} is the mass of the tip fixture, and I_{tip} is its moment of inertia evaluated with respect to the axis that coincides with the elastic axis of the beam.

Equations (3a) and (3c) prescribe the shear force equality at the tip in the z and y direction, respectively. The underlined terms in these two equations capture the contribution of tendon-induced forces in the shear directions. These terms are invariant to the position of the tendon (they do not depend on e_y or e_z) and were also used in [21, 22, 26, 27] for the beam-tendon systems and approximated in [28, 29] for a compressively loaded blade. Equations (3b) and (3d) represent the bending moments acting on the beam. In these two equations, the crossed terms represent the bending moments caused by the static axial force that are neglected in the following analysis. This is in line with the previous assumption that the deflections caused by the static bending moments can be neglected. Equations (3e) and (3f) prescribe the torque and warping at the tip of the beam, respectively. The latter condition was not included in the previous studies [21, 22, 26–29] as the effect of warping was assumed to be negligible. In the former equation, the underlined terms relate to the additional moments that are introduced by the shear forces of the eccentrically placed tendon. Both of these terms disappear when the tendon is placed in the elastic axis (these terms cannot be found in the previous studies of beam-tendon systems). It is interesting to note that Eq. (3e) introduces the coupling between the lead-lag motion and torsion when the tendon is not placed on the axis of symmetry of the cross-section, i.e. $e_z \neq 0$. For a general placement of the tendon, so that $e_y \neq 0$, $e_y \neq y_0$ and $e_z \neq 0$, there would be coupling between flapping, lead-lag and torsion motions of the beam even if its cross-section is symmetric. Finally, Eqs. (3g) and (3h) enforce the same tip displacements of the beam and the tendon in the z and y, respectively. These conditions reduce to the corresponding conditions in [21, 26] when the tendon is placed in the elastic axis. Due to these coupling conditions, the motion of the beam drives the motion of the tendon which, in turn, influences the beam by applying the axial force. This is the reason for an interaction between the modes of the beam and the tendon.

The derivation of the EoM and BCs without the coupling terms provided by beam-tendon interaction can be found in [8, 9, 15] and the coupling boundary conditions can be derived as described in the following. In Fig. 2(a) a deformed cross-section can be seen. During motion, the cross-section undergoes translation,

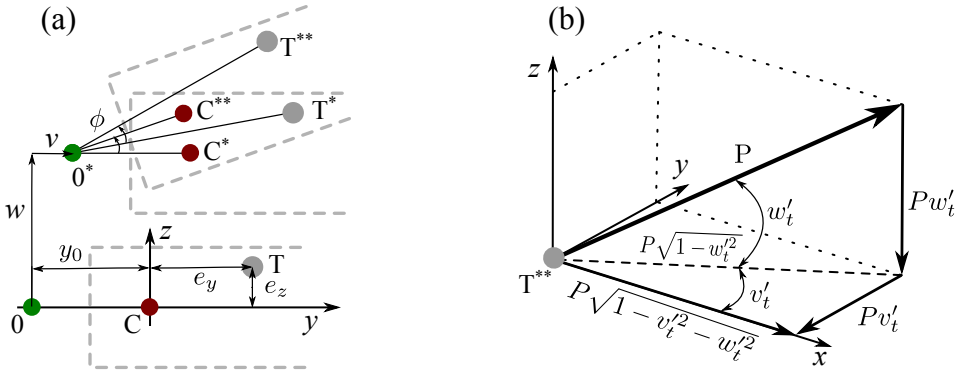

Figure 2: The origin of the coupling boundary conditions: (a) the geometric coupling between the beam and the tendon, and (b) the loading conditions

which is defined by the displacement v and w of the shear centre 0, and rotation about the shear centre defined by ϕ. During translation, the shear centre 0 moves to 0^*, and the tendon moves from its original position T to T^*. During rotation, the position of the shear centre remains unchanged while the tendon moves to T^{**}. The final position the tendon can be therefore written as [9, 15]

$$v_t = v - e_z \sin\phi \approx v_t = v - e_z\phi$$

$$w_t = w - (y_0 - e_y)\sin\phi \approx w_t = w - (y_0 - e_y)\phi$$

in which the angle ϕ was considered to be a small quantity. As a sanity check, it can be seen from Fig. 2(a) that for the positive rotation of the cross-section, the tendon moves in the negative direction of the y axis and the positive direction of the z axis, which agrees with the derived equations.

The tendon-induced shear forces contributions to Eqs. (3a) and (3c) can be deduced based on Fig. 2(b). After deformation, the tendon's slope at the tip is not equal to the slope of the beam. The applied force P is not perpendicular to the tip plane of the beam and its direction is determined by the slope of the tendon. Therefore, in order to obtain the shear and axial forces acting on the beam, the applied force P must be decomposed into the original undeformed directions as shown in Fig. 2(b). The contribution to the shear forces in the y and z directions can be found as Pw_t' and Pv_t' respectively and the axial component of the force is given by $P\sqrt{1-v_t'^2-w_t'^2} \approx P$. In these expressions, w_t' and v_t' were considered as small quantities.

Equations (1)-(3) create a system of three forth-order and two second-order partial differential equations with the corresponding number of boundary conditions. All these equations must be solved simultaneously as there is coupling between the motions of the beam and the tendon due to asymmetry of the beam's cross-section and the connection between the tendon and the beam.

2.1.1. Numerical free vibration analysis

In order to evaluate the modal properties (natural frequencies and mode shapes) of the beam-tendon system, the same procedure as in [21, 24] is used. The excitation forces and moments in Eq. (1) are set to zero and an assumption of the normal mode is used. Therefore, a solution of any given dependent variable is expressed as the multiplication of the time-invariant mode shape and the time-varying harmonic function of the constant frequency in the following form

$$\begin{gathered} w(t,x) = W(x)\mathrm{e}^{\mathrm{i}\omega t}, \quad v(t,x) = V(x)\mathrm{e}^{\mathrm{i}\omega t}, \quad \phi(t,x) = \Phi(x)\mathrm{e}^{\mathrm{i}\omega t}, \\ w_{\mathrm{t}}(t,x) = W_{\mathrm{t}}(x)\mathrm{e}^{\mathrm{i}\omega t}, \quad v_{\mathrm{t}}(t,x) = V_{\mathrm{t}}(x)\mathrm{e}^{\mathrm{i}\omega t}, \end{gathered} \tag{4}$$

where ω is the angular natural frequency, and $W(x), V(x), \Phi(x), W_t(x), V_t(x)$ are the components of the mode shape which represent, respectively, the bending in the z and y directions, the rotation about the elastic axis, and the transversal motion of the tendon in the z and y directions. The complete mode shape of the system can then be formally written as $\Psi(x) = [W(x), V(x), \Phi(x), W_t(x), V_t(x)]$. In the rest of the paper, if the mode shape is dominated by the motion of the beam, it will be refer to as a beam-dominated mode. On the other hand, if the mode shape is determined by the tendon activity, the term tendon-dominated mode will be used instead.

As in the previous studies [21, 24], substituting the normal mode forms into Eqs. (1), (2) and (3) allows one to eliminate time and rewrite the PDEs into a system of first order ordinary differential equations (ODEs) that, together with the BCs, define a boundary value problem. This boundary value problem is then solved by a Matlab bvp4c solver [30] for the unknown natural frequencies ω and corresponding mode shape components $W(x)$, $V(x)$, $\phi(x)$, $W_{\mathrm{t}}(x)$ and $V_{\mathrm{t}}(x)$. This solver is very versatile since it uses a collocation method but may suffer from a decreased numerical performance if an appropriate starting guess is not provided.

In order to obtain an appropriate starting guess, the following process, which is similar to the one used in [28], was implemented. Instead of removing the excitation forces and moments in Eq. (1), the harmonic excitation is assumed. By submitting the harmonic response from Eq. (4) to the system of equations with the harmonic forcing, a slightly different boundary value problem can be defined. In this boundary value problem, the excitation frequency ω is known and the response $W(x)$, $V(x)$, $\phi(x)$, $W_{\mathrm{t}}(x)$ and $V_{\mathrm{t}}(x)$ can be evaluated from any non-zero starting guess easily. The natural frequencies and the mode shapes can then be approximately estimated from the obtained responses and used as the initial guesses to evaluate the natural frequencies and mode shapes accurately.

The results obtained by the described numerical procedure from the proposed analytical equations of motion will be referred to as "theoretical results" in the rest of the paper. In contrast, the results obtained from the finite element model described in the following section will be referred to as "numerical results". It is noted that the theoretical results are of higher importance since they originate from the novel mathematical description of the system. The finite element model is not considered to be a novel aspect of this study

(although it describes previously unstudied system) and it is meant to merely complement the experiment in validating the proposed theoretical model.

2.2. Finite element model

In addition to the experimental validation, a finite element (FE) model of the system is used to further validate the proposed theoretical model for high applied forces that cannot be achieved in the experiment and to put the observed discrepancies between the computed and experimental results into perspective. It is not claimed that the used finite element model is a novel aspect of the study and it should not be perceived as such. The finite element model is present merely for the mentioned validation purposes. The model is build and analysed in Abaqus CEA [31]. The beam and the tip fixture are modelled using linear shell elements and the tendon using linear truss elements. The meshes of the beam, tip mass and tendon are rigidly connected so there is no relative motion between them. In order to obtain the modal parameters of the beam-tendon system, a two step procedure was carried out. Firstly, the axial force was applied to the tendon and the static deformed position of the beam-tendon system was found. Then, the modal characteristics were evaluated for this new deformed configuration of the system. Therefore, unlike in the theoretical model, the deflection caused by the static axial force was not neglected in the FE model. The FE model allows the effect of the position of the tendon and its tension on the modal characteristics of the system to be studied and compared to the experimental and theoretical results.

3. Experimental verification of free vibration analysis

In this section, the experimental validation of the results of the theoretical and numerical free vibration analysis is presented. Firstly, the experimental system configuration is described, then the frequency-loading diagrams of three selected configurations are used to thoroughly validate the theoretical model.

3.1. Experimental set-up description

The experimental set-up can be seen in Fig. 3. A similar experimental set-up to test the beam-tendon systems was already used in [21, 24, 27]. It features a channel section aluminium beam which is rigidly clamped at one end and free at the other, and is axially loaded by a steel cable. The tendon is attached to the tip using a rigid tip fixture which enable various tendon locations (as seen in the left inset in Fig. 3 in which "s.c." stands for the shear centre, and "c.g." for the centre of gravity). The tendon then passes inside or outside of the beam towards the clamp, but it is always parallel to the beam's original position. This is ensured by an acrylic tendon guide which is placed close to the clamp (as seen in the right inset in Fig. 3). This guide also limits the active length of the tendon to the same length as the beam, so the experimental system represents the system shown in Fig. 1 and can therefore be modelled using the proposed theoretical model. The tendon then continues through the clamp and pulley and is attached to a hanging platform. The tension in the tendon, and hence the axial load applied to the beam, is controlled by the amount of weight placed on the platform.

The beam was excited using a modal shaker controlled via a modular control and data acquisition (DAQ) system. Random excitation was used to excite the frequency range between 5 and 450 Hz and the response data were recorded using a two small uni-directional accelerometers located close to the tip of the beam. The load was varied using the weights placed on the hanging platform in two kilogram increments from 2kg to up to 90kg. The response data and the input force were used to estimate the FRFs using the H_v-estimator [32] and the natural frequencies were estimated using the least-square complex frequency (LSCF) estimator [33]. Several locations of the tendon are experimentally investigated as marked in the left inset in Fig. 3. For locations 3 (centre of gravity) the measurement was performed firstly in the z direction and then in the y direction by rotating the beam in the clamp by 90 degrees (the shaker remained vertical). For locations 1, 2 (shear centre), 4 and 5 the measurement was only performed in the z direction since in the y direction, the tendon would collide with the stinger or it would not be possible to lead it through the clamp.

The nominal parameters describing the beam-tendon system are as follows. The web height of the channel cross-section is equal to 0.5 in = 12.7 mm, the flange length is 1 in = 25.4 mm and the wall thickness

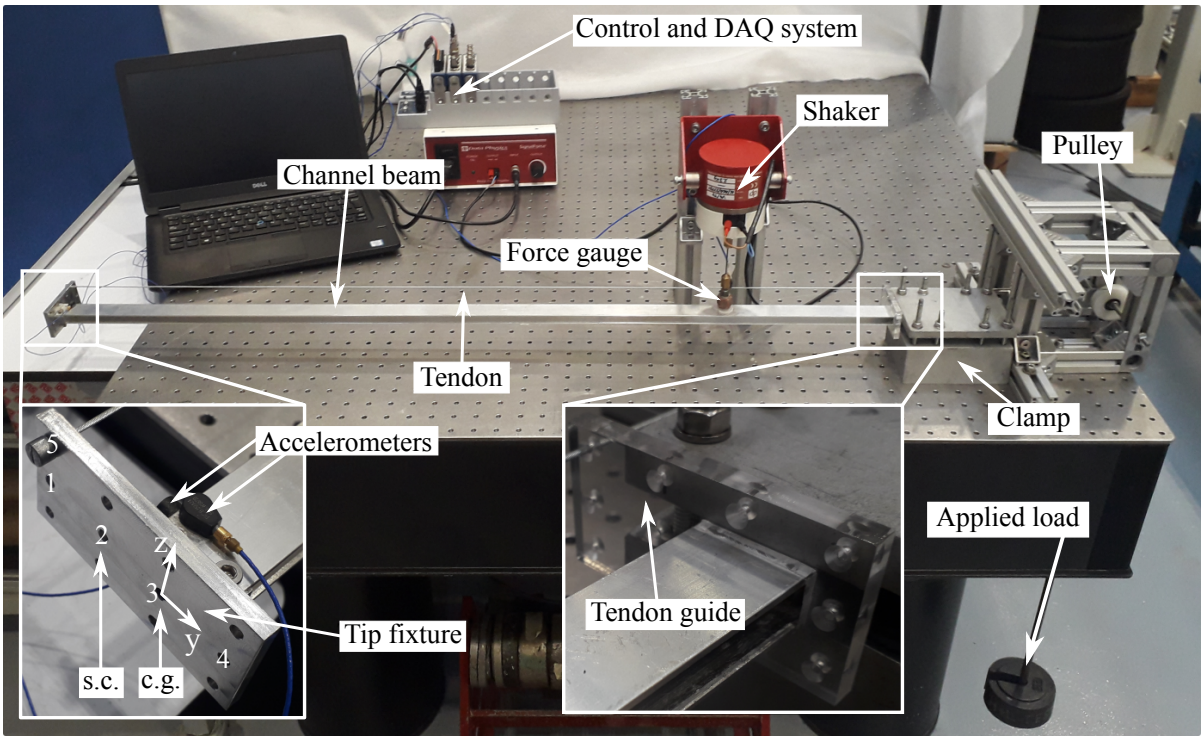

Figure 3: Experimental set-up. A channel section beam subjected to the tendon-induced axial force generated by the applied load is excited by a shaker to obtain frequency response functions for estimation of the modal properties which are then used to validate the theoretical model.

is 16 swg = 1.626 mm. From these parameters, the cross-sectional characteristics can be computed as in [9] and are equal to $I_z = 2.6649 \times 10^{-9}\,\mathrm{m}^4$, $I_y = 6.2746 \times 10^{-9}\,\mathrm{m}^4$, $J = 8.8664 \times 10^{-11}\,\mathrm{m}^4$, $y_0 = -0.0219m$, $\Gamma = 1.6382 \times 10^{-13}\,\mathrm{m}^6$, $r_c^2 = 5.6923 \times 10^{-4}\,\mathrm{m}^2$ and $\beta_y = 0.0459\,\mathrm{m}$. The length of the beam is $L = 1\,\mathrm{m}$ and its weight per unit length is $m = 0.259\,\mathrm{kg\,m}^{-1}$. The beam is made of aluminium with the nominal Young's modulus equal to $E = 69.5\,\mathrm{GPa}$ and Poison's ratio $\mu = 0.3$. The tip fixtures can be weighted so its mass is known and equal to $M_{\mathrm{tip}} = 45\,\mathrm{g}$ (the weight of accelerometers is included) and its moment of inertia can be approximately estimated as $I_{\mathrm{tip}} = 7.9101 \times 10^{-7}\,\mathrm{kgm}^2$. The tendon mass is equal to $m_t = 0.011\,\mathrm{kg\,m}^{-1}$.

3.2. Under-lying beam model updating

Before including the tendon into the experiment, the theoretical and numerical models of the beam with and without the tip mass were validated. The purpose of this step was to obtain the underlying model of the beam as accurately as possible so that the effect of the tendon can be studied separately. In the previous studies [21, 24, 27] it was observed that the errors in the under-lying beam model propagate to the beam-tendon system, and lead to inaccuracies between the measured and computed frequency-loading diagrams. The modal properties of the beam were obtained by the impact hammer testing, where two accelerometers at the tip were used to acquire the response data, and the roving hammer technique applied to excite the beam in various span locations. The modal properties were estimated from the measured FRFs using the least-square complex frequency (LSCF) estimator [33].

In order to compare the theoretical, numerical and experimental mode shapes, they all have to be expressed in the same location of the beam. The two accelerometers collecting the experimental data were placed approximately 4mm from the upper corner of the beam (see the left inset in Fig. 3) and roving hammer excitation was also applied along the edge. Therefore, the mode shape values from the finite element model were also estimated along the same edge. In order to compare the theoretical mode shapes with the experiment, the theoretical mode shape, which is computed with respect to the elastic axis, was

transferred to the place of the measurement as follows

$$\overline{W}(x) = W(x) + y_a\Phi(x), \quad \text{and} \quad \overline{V}(x) = V(x) - z_a\Phi(x), \tag{5}$$

where $\overline{W}$ and $\overline{V}$ are the theoretical mode shapes evaluated in the measurement location, y_a is the y distance between the elastic axis and the location of the accelerometer which measures the flapping (vertical) motion ($y_a = 15\,\text{mm}$) and z_a is the z distance between the elastic axis and the accelerometer which measures in the lead-lag (horizontal) motion ($z_a = 2.3\,\text{mm}$).

3.2.1. Under-lying beam model without the tip mass

The comparison of the experimental and computed natural frequencies (using the nominal parameters from section 3.1) is given in Tab. 1 and visualised in Fig. 4(a). From this table, it can be seen that there

	f^{exp} [Hz]	f^{ABQ} [Hz]	error [%]	f^{BM} [Hz]	error [%]	f^{BMW} [Hz]	error [%]
1: 1F	12.77	13.82	8.21	13.77	7.82	13.91	8.90
2: 1L	21.22	22.73	7.12	22.96	8.2	22.96	8.20
3: 2F	59.86	62.25	3.99	57.47	-3.99	63.09	5.40
4: 1T	98.56	103.28	4.89	104.20	5.71	106.24	7.79
5: 2L	132.38	141.91	7.20	143.90	8.70	143.90	8.70
6: 3F	145.76	148.65	1.99	130.17	-10.69	150.79	3.45
7: 4F	245.13	248.70	1.45	202.35	-17.45	252.85	3.15
8: 2T	318.10	336.53	5.79	353.04	10.99	346.52	8.94
9: F5	367.46	378.34	2.96	263.01	-28.42	389.53	6.01
10: L3	371.14	394.90	6.40	402.92	8.56	402.92	8.56
$\Sigma\|\text{error}\|/10$			**5.00**		**14.36**		**6.91**

Table 1: Comparison of the natural frequencies of the beam without the tip when described by nominal parameters. f^{exp} represents the experimentally measured natural frequencies, f^{ABQ} represents the results obtained by the finite element model, f^{BM} represents the results from the beam model without warping, and f^{BMW} denotes the natural frequencies of the beam model with warping. iF marks the i^{th} vibration mode dominated by the flapping motion, iL marks the i^{th} mode dominated by the lead-lag motion, and iT stands for the i^{th} mode driven by the torsion of the beam.

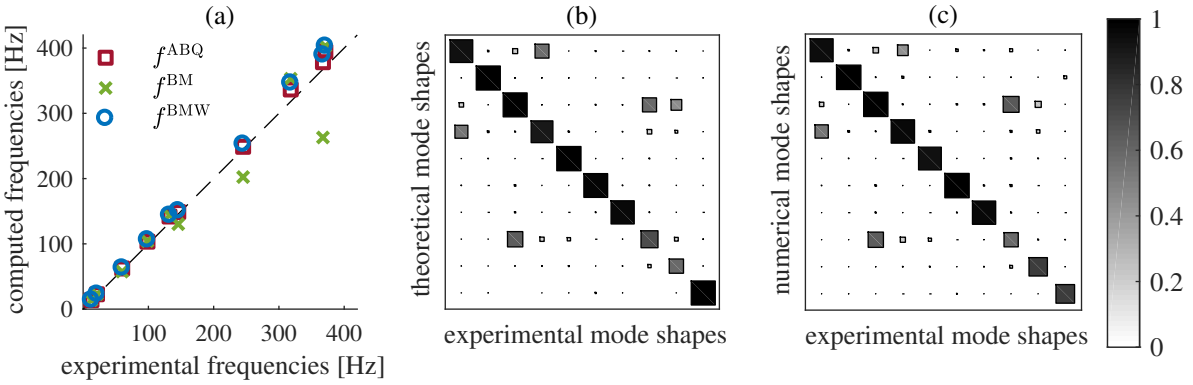

Figure 4: The beam with the nominal parameters without the tip mass: (a) natural frequencies comparison, (b) MAC between the experimental and theoretical (BMW) mode shapes, and (c) MAC between the experimental and numerical mode shapes

are ten vibration modes with the natural frequencies lower than 400 Hz. Five of them are dominated by the flapping motion (marked by iF), three of them by the lead-lag motion (marked by iL) and two of them by the torsion (marked by iT). The average absolute error is also included in Tab. 1. It can be seen that average error of the FE model and the beam model with warping are similar, being 5 % and 6.91 %, respectively.

On the other hand, the error of the beam model without warping is much higher, over 14 %. This indicates that the warping must be included in the theoretical model in order to describe the free vibration of the beam accurately. This fact is also reinforced by the graphical comparison of natural frequencies in Fig. 4(a) where it can be clearly seen that while the natural frequencies obtained from the FE model and the model with warping are well correlated with the experimental ones, the beam model without warping significantly diverges from the experimental values. The modal assurance criteria (MAC) between the measured and computed mode shapes for the nominal parameters can be seen in Fig. 4(b) and Fig. 4(c). Since all MAC values are very high, it can be concluded that both the FE model and the theoretical beam model with warping describe the mode shapes of the system very well.

Although the modal parameters are well represented by the used model, it was decided to further reduce the error in the natural frequencies by updating the Young's modulus of the beam. This was driven by the observations from previous studies [21, 24, 27] where the errors in the under-lying beam models led to discrepancies in the results for the full beam-tendon system. It is therefore desired to reduce the relative error of the beam's natural frequencies as much as possible for all frequencies in the investigated frequency band. To this end, the value of the Young's modulus was optimised using the following objective function

$$E^{\mathrm{upd}} = \underset{E}{\operatorname{argmin}} \frac{1}{N_m} \sum_{i=1}^{N_m} \left| 1 - \frac{f_i^{\mathrm{exp}}}{f_i^{\mathrm{comp}}(E)} \right|, \tag{6}$$

where N_m is the number of considered mode shapes ($N_m = 10$), and f^{comp} is the computed natural frequency obtained either from the FE model or the beam model with warping. The optimisation showed that in order to obtain the minimal error for the FE model, the updated Young's modules must be equal to $E^{\mathrm{ABQ}} = 0.9025E$, whereas for the beam model, it is $E^{\mathrm{BMW}} = 0.8607E$. The resulting natural frequencies and corresponding errors are written in Tab. 2 and visualised in Fig. 5(a). It can be seen that average errors

	f^{exp} [Hz]	$\mathrm{f}^{\mathrm{ABQ}}$ [Hz]	error [%]	$\mathrm{f}^{\mathrm{BMW}}$ [Hz]	error [%]
1: 1F	12.77	13.13	2.80	12.90	1.03
2: 1L	21.22	21.60	1.76	21.30	0.38
3: 2F	59.86	59.14	-1.21	58.53	-2.22
4: 1T	98.56	98.22	-0.35	98.57	0.00
5: 2L	132.38	134.81	1.84	133.50	0.85
6: 3F	145.76	141.22	-3.11	139.89	-4.02
7: 4F	245.13	236.26	-3.62	234.58	-4.31
8: 2T	318.10	319.70	0.50	321.48	1.06
9: F5	367.46	359.43	-2.19	361.38	-1.65
10: L3	371.14	375.22	1.08	373.81	0.72
Σ|error|/10			**1.84**		**1.62**

Table 2: Comparison of the natural frequencies of the beam without the tip described by the updated parameters

of both models have decreased and the error of the beam model is even lower than that of the FE model, being 1.62 % and 1.84 %, respectively. While the natural frequencies improved, no detrimental changes can be seen in the MAC values in Fig. 5(b) and Fig. 5(c). Therefore, the optimised Young's moduli will be used in the rest of the paper.

In addition to the MAC values, the modes shapes are graphically compared in Fig. 6, and the same set of mode shapes from the FE model can be seen in Fig. A.17. It can be seen that the match between all three sets of mode shapes is very good. The biggest discrepancies can be observed in the torsional modes (Fig. A.17(d) and Fig. A.17(h)) where it is seen that the values of experimental mode shapes in the y direction do not agree with the prediction of the theoretical and numerical models. Since both models gave the same results, it is concluded that the experimental torsional mode shapes have not been accurately estimated from the measured FRFs. This is most likely caused by their weak excitation during the impact hammer testing. Due to the small size of the cross-section, it was not possible to excite them properly.

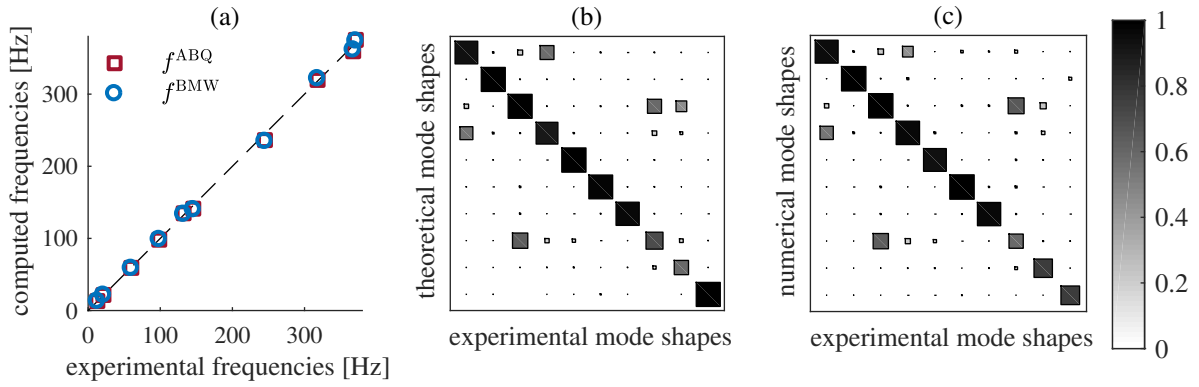

Figure 5: The beam with the updated parameters and the tip mass: (a) natural frequencies comparison, (b) MAC between the experimental and theoretical mode shapes, and (c) MAC between the experimental and numerical mode shapes

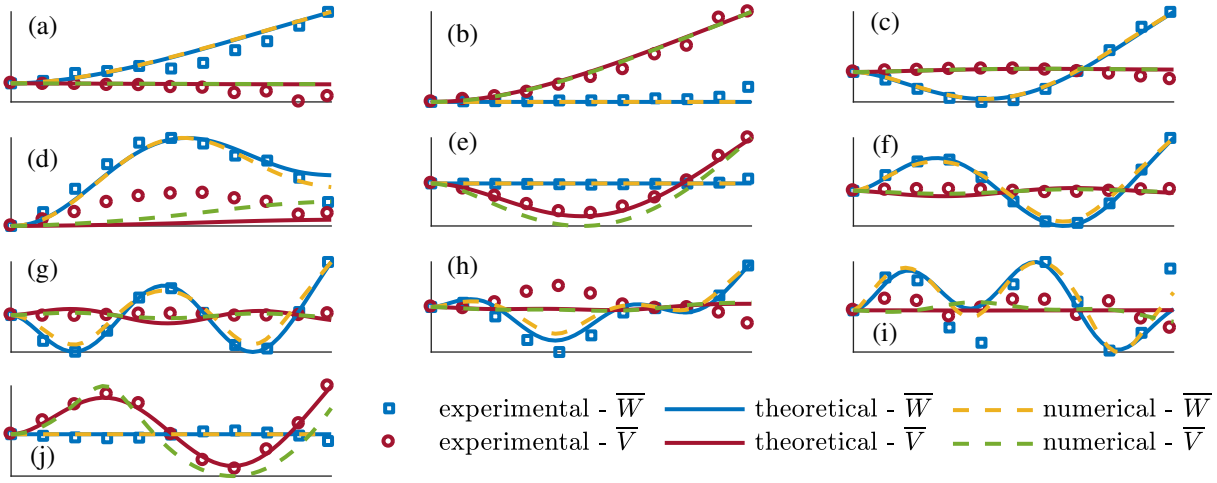

Figure 6: Comparison of the mode shapes for the beam without the tip mass: (a) the first flapping (out-of-plane bending) mode - 1F, (b) the first lead-lag (in-plate bending) mode - 1L, (c) 2F, (d) the first torsion mode - 1T, (e) 2L, (f) 3F, (g) 4F, (h) 2T, (i) F5, (j) L3. The same sets of mode shapes obtained from the finite element model can be seen in Fig. A.17.

3.2.2. Under-lying beam model with the tip mass

Having obtained the parameters of the beam without the tip mass, the tip fixture was mounted on the beam and experimental modal analysis using the impact hammer was repeated. In this section, the experimental results are compared with the theoretical and numerical models augmented by a tip mass. The mass of the tip fixture (including the accelerometers) could be weighted, but its moment of inertia, needed for the theoretical model, could be only approximately estimated. Therefore, in order to improve the correlation between the theoretical and experimental results, the moment of inertia was optimised (using the same objective function as for the Young's modulus). The resulting final moment of inertia was found to be $I_{tip}^{upd} = 0.1366 I_{tip}^{nom}$. In the FE model, no optimisation was performed. It was only ensured that the mass of the tip attachment modelled matches the physical mass accurately.

The comparison of the computed and experimental natural frequencies, and their relative errors is given in Tab. 3 and visualised in Fig. 7(a). It can be seen that the average error of both models increased by approximately 2 % compared to the updated beam without the tip mass. While the numerical and theoretical model led to similar average error, there are differences in errors of each mode. Most notably, the error of the second flapping mode of the theoretical model is over 15 % while the finite element model's error is less than 1 %. Both model also gave larger errors for the natural frequency of the first torsion model, being

	f^{exp} [Hz]	f^{ABQ} [Hz]	error [%]	f^{BMW} [Hz]	error [%]
1: 1F	10.12	10.25	1.25	10.35	2.28
2: 1L	16.49	15.33	-7.03	16.23	-1.00
3: 1T	43.27	39.90	-7.79	38.25	-11.61
4: 2F	63.39	63.72	0.82	73.63	16.14
5: 2L	111.89	105.09	-6.08	111.72	-0.15
6: 3F	131.90	132.01	0.08	132.13	0.18
7: 4F	226.98	227.25	0.12	222.16	-2.12
8: 2T	239.52	244.45	2.05	239.52	0.00
9: 3L	323.50	305.59	-5.66	326.73	1.00
10: 5F	340.44	344.59	1.21	332.72	-2.27
Σ|error|/10			**3.21**		**3.99**

Table 3: Comparison of the natural frequencies of the beam with the tip mass

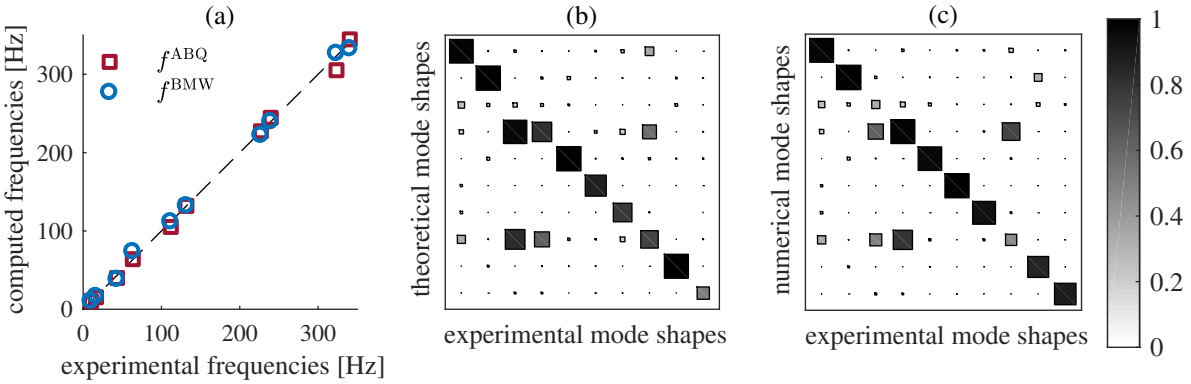

Figure 7: The beam with the updated parameters and the tip mass: (a) natural frequencies comparison, (b) MAC between the experimental and theoretical mode shapes, and (c) MAC between the experimental and numerical mode shapes

almost $-8\,\%$ for the numerical model, and almost $-12\,\%$ for the theoretical model. Despite these errors, both models correctly captured the changes in the natural frequencies caused by the present the tip mass. In particular, the frequencies of the bending modes have decreased due to additional mass at the tip and the order of the modes changed. The first torsional mode's natural frequency changed significantly due to the presence of the tip fixture with large moment of inertia so the torsional mode moved to the third position. Since all these changes were captured adequately by the theoretical and numerical model, these models are considered as validated and are used in the following study of the beam-tendon system.

The corresponding MAC can be found Fig. 7(b) and Fig. 7(c), and the visual comparison of the mode shapes in Fig. 8, and the same set of mode shapes from the FE model can be seen in Fig. A.18. As in the previous case, a good overall correlation between the three sets can be seen. However, there are some differences that are worth noting. The largest errors can be observed in the MAC value related to the torsional modes. Since numerical and theoretical results correspond to each other well, it is likely that the torsional modes (Fig. 8(c) and Fig. 8(h)) have not been estimated accurately from the experiment, which caused small MAC values as seen in Fig. 7. The poor estimation was probably caused by insufficient excitation of the torsional modes during the impact hammer testing due to a small cross-section which makes it difficult to excite torsion. Since there is also coupling between bending and torsion, the first torsional mode and the second flapping one look very similar and this is also reflected in the MAC values. In Fig. 8(j) it can be seen that the theoretical model incorrectly predicted the motion of the y direction. The reason for this has not been further investigated as all other modes are predicted correctly.

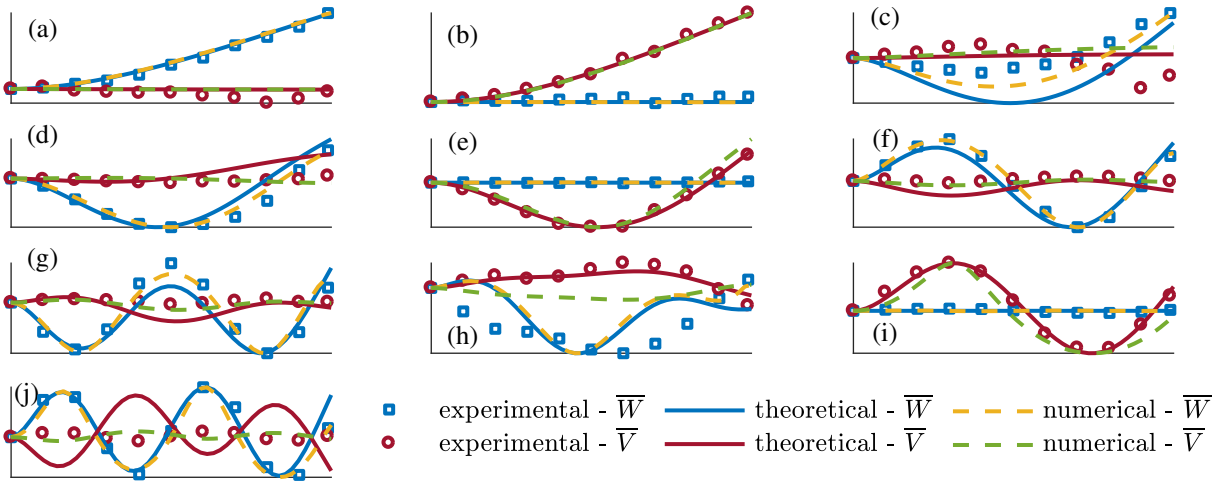

Figure 8: Comparison of the mode shapes for the beam with the tip mass: (a) the first flapping (out-of-plane bending) mode - 1F, (b) the first lead-lag (in-plate bending) mode - 1L, (c) the first torsion mode - 1T, (c) 2F, (e) 2L, (f) 3F, (g) 4F, (h) 2T, (i) 3L, (j) 5F. The same sets of mode shapes obtained from the finite element model can be seen in Fig. A.18.

3.3. The beam-tendon system

In the previous section, the under-lying theoretical and numerical beam models were carefully validated and updated against the experimental results. In this section, the full beam-tendon system is investigated. The frequency-loading diagrams of the three selected tendon locations are investigated in detail and compared with the numerical and theoretical results.

3.3.1. The tendon placed in the shear centre

In the first investigated case, the tendon was placed in the shear centre of the channel cross-section (location 2 in the left inset in Fig. 3). It was therefore located outside of the cross-section, and its coordinates in the theoretical model were $e_y = y_0$ ($y_0 < 0$) and $e_z = 0$. The comparison of the experimental, numerical and theoretical frequency-loading diagrams can be seen in Fig. 9. Since it was not possible to perform the measurements in both directions, only the results from the measurement in the z direction are shown. Therefore, some modes that are dominated by the motion in the y direction are not excited very well, so the corresponding natural frequencies may not be very accurate. As in the previous studies [21, 24] two sets of frequency loci can be distinguished. The frequency curves that are almost parallel to the x-axis represent the vibration modes which are dominated by the motion of the beam. Thus, they are termed as beam-dominated modes. On the other hand, the frequency loci that are increasing rapidly with the applied force represent the tendon-dominated modes that are driven by the motion of the tendon. These two sets of modes interact with each other through the frequency loci veering since the beam and tendon are coupled via their connection at the tip of the beam.

The agreement between the computed and experimental results can be considered as satisfactory. The level of discrepancy is similar to the previous experimental studies [21, 24] and it is given by the error in the under-lying beam models' natural frequencies. It can be observed that while the experimental tendon-dominated modes are very well matched by the theoretical and numerical model, there is an approximately constant offset in the computed and measured beam-dominated modes. Despite this offset, their rate of change (the frequency shift due the applied axial loading) is well represented. It can be also noticed that the mode with the natural frequency just under 250 Hz has not been captured in the experiment. This is the eighth mode, which represent the second torsional mode, and has not been excited properly by the shaker. While the mode is missing in the experimental results, the theoretical and numerical models predict it and their results can be considered as equivalent. Their difference is given by the differences in the under-lying beam models. Table 3 shows that the finite element model over-predicts the natural frequency of the second

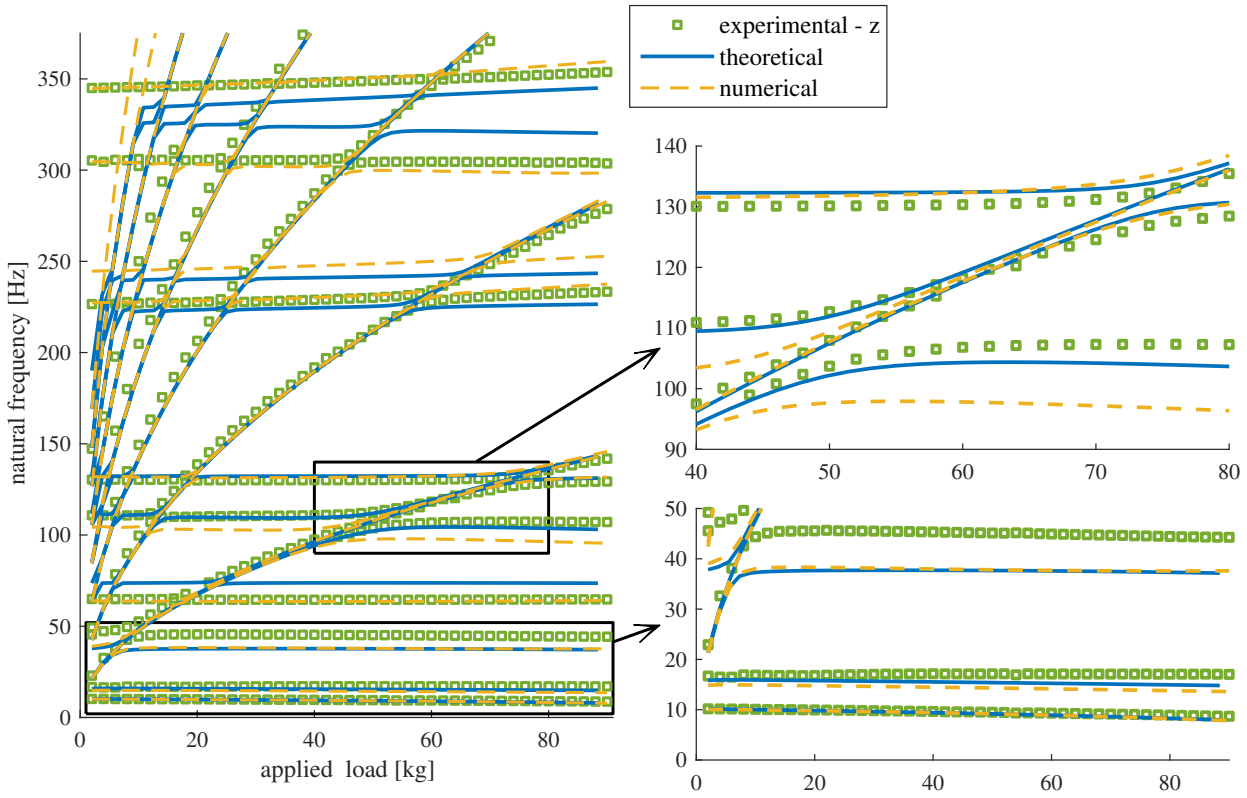

Figure 9: The frequency-loading diagram for the beam-tendon system with the tendon located in the shear centre of the cross-section.

torsion mode by 2 % while the theoretical model gives negligible error. These errors then propagate into the beam-tendon system and so the numerical results show higher frequency for this mode.

It can be noticed that each beam-dominated mode is influenced differently by the applied axial load. Some natural frequencies remain practically constant while some of them decrease. However, it can be also seen that the natural frequency of the highest mode (which represent the fifth flapping mode) is increasing with the applied axial loading. This is caused by the location of the tendon in the shear centre and will be discussed in detail in section 4.1. The veering region depicted in the detail in Fig. 9 is also very well represented by both the numerical and theoretical model. It can be noticed that some experimental values are missing. The missing natural frequencies are associated with the motion of the system in the y direction, which has not been properly excited for the present case since it was not possible to place the shaker so that it would not collide with the tendon in the y direction. Therefore, a detailed discussion of veering will be given for the other two cases, in which the veering region were better experimentally characterised.

3.3.2. The tendon placed in the centre of gravity

In the second case, the tendon was located in the centre of gravity of the channel cross-section as indicated by point 3 in the left inset of Fig. 3. Therefore, the coordinates of the tendon were $e_y = 0$ and $e_z = 0$. The comparison of experimental, theoretical and numerical frequency-loading diagrams can be seen in Fig. 10. Since it was possible to perform the measurements in both directions, two sets of experimental results are given. The green square markers represent the results measured in the z direction, while the red circles are the results measured in the y direction. As in the previous case, two sets of modes - the beam-dominated and tendon-dominated modes - can be seen. The agreement between the experimental and computed results is again satisfactory, and the observed discrepancies originate in the error of the under-lying beam model. As in the previous case, the second torsion mode has not be excited in the experiment. Each mode exhibits

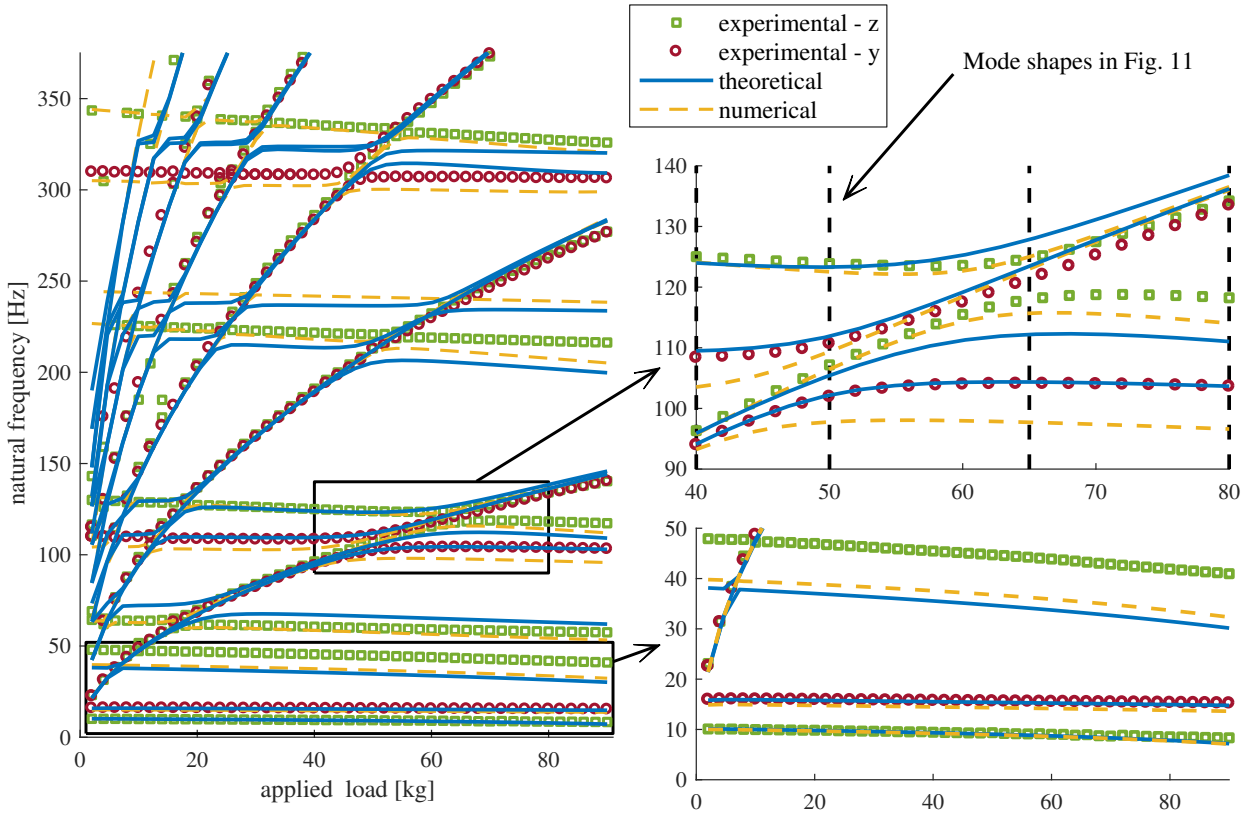

Figure 10: The frequency-loading diagram for the beam-tendon system with the tendon located in the centre of gravity of the cross-section.

different frequency shift due to the applied axial loaded, but none of them is seen to increase. This is caused by the location of the tendon in the centre of gravity and will be further discussed in section 4.1.

Two sets of tendon-dominated modes have been excited in the experiment - one corresponding to the motion of the tendon in the z direction and the other one in the y direction. It can be seen that the frequency loci of these modes overlay very well when not influenced by veering with the beam-dominated modes. This is given by the symmetry of the tendon's circular cross-section. Depending on the nature of the modes involved, some modes veer with each other while other modes are not influenced and pass through the veering region unaffected. This behaviour is depicted in detail in Fig. 10 and also visualised by the theoretical mode shapes in Fig. 11 and numerical mode shapes in Fig. A.19. There are two veering regions seen in this highlighted region. The first veering region is between 40 kg and 55 kg and involves the second lead-lag bending mode and the first tendon-dominated mode in the the y direction as seen from the corresponding mode shapes. While at 40 kg (before the veering region) the natural frequency of the tendon-dominated mode is lower than the natural frequency of the beam-dominated mode, at 65 kg (after the veering region) the opposite is true. The mode shapes of these two modes have swapped during the veering and the phase changed as is typical for the veering phenomena [34, 35]. The first tendon-dominated mode in the z direction (the green markers) passes through the first veering region unaffected, and its mode shape is not influenced. This is given by the fact that there is no coupling between the motion in the z and y direction when the tendon is placed in the centre of gravity. In the second veering region, between approximately 60 kg and 70 kg the veering occurs between the six mode of the beam, which is a coupled bending-torsion mode termed as the third flapping mode (3F) in the previous text, and the first tendon-dominated mode in the z direction which previously passed the first veering region unaffected. Once again, typical features of the veering can be observed, i.e. the mode shapes swap and their phase changes, and the

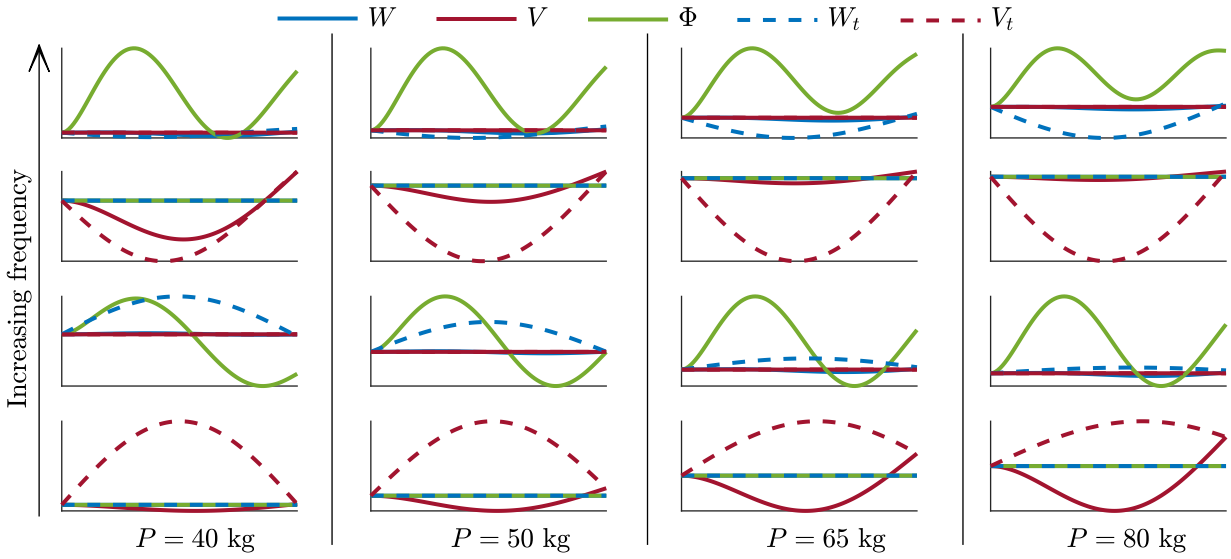

Figure 11: Theoretical mode shape variations during veering for the beam-tendon system with the tendon placed in the centre of gravity. Corresponding mode shapes of the finite element model can be found in Fig. A.19.

tendon-dominated mode which is not coupled with the z direction passes the veering region unaffected.

3.3.3. The tendon placed in a general location

In the third case, the tendon was located in location 5 as marked in the left inset of Fig. 3. The location does not lie on the axis of symmetry and is far from the centre of gravity of the cross-section. Due to this fact, the static tendon loading causes large bending moments that significantly deflect the beam. Therefore, it was only possible to perform the experiments in a range between 2 kg and 60 kg. In the theoretical model, $e_y = 2y_0$ ($y_0 < 0$) and $e_z = h$, where h is the web height of the channel cross-section. The comparison of the experimental, theoretical and numerical frequency-loading diagrams can be seen in Fig. 12. Again, two sets of vibration modes - the beam-dominated and tendon-dominated ones - can be observed. As in the previous cases, the comparison of all three data sets is satisfactory and the discrepancies can be attributed to the errors in the under-lying beam models. This means that the proposed theoretical model is able to describe the situation in which the tendon is placed off the axis of symmetry accurately.

From the theoretical model, specifically from Eq. (3e), it can be seen that when $e_z \neq 0$ there is a coupling between the y direction bending and torsion. This coupling is then responsible for the appearance of the veering region detailed in Fig. 12. The corresponding theoretical and numerical mode shapes can be seen in Fig. 13 and Fig. A.20, respectively. When the tendon was placed in the centre of gravity, there were tendon-dominated modes passing through the veering regions. These modes were not affected by the veering because they were not coupled to the modes that veered with each other. In contrast, for the present case, all modes are mutually coupled together and all of them are affected by the veering. From Fig. 13, it can be seen that the tendon moves simultaneously in both bending directions due to the aforementioned coupling. Typical features of veering can also be seen. For example, the third mode (counted from the bottom) at $P = 35$ kg represents the second lead-lag mode which is already coupled with the torsion due to the eccentric placement of the tendon. This mode than veers with both tendon-dominated modes, therefore becoming the first mode (the very bottom one) at $P = 60$ kg. Similarly, the tendon-dominated mode that is the first at $P = 35$ kg veers with the other modes and becomes the third mode at $P = 60$ kg while the phase of its component changes. The upper row of the mode shapes in Fig. 13, which represent the third flapping mode does not change since its frequency loci is far away from the other modes.

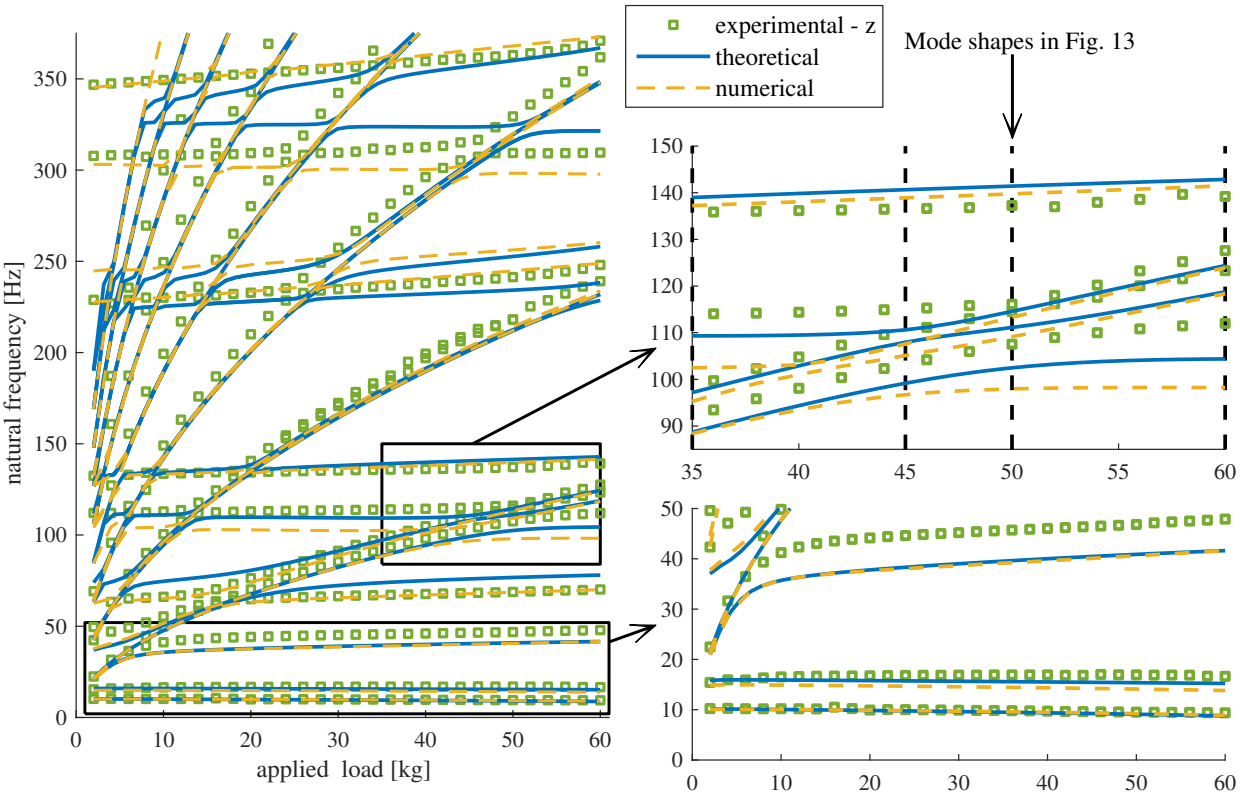

Figure 12: The frequency-loading diagram for the beam-tendon system with the tendon located in a general location.

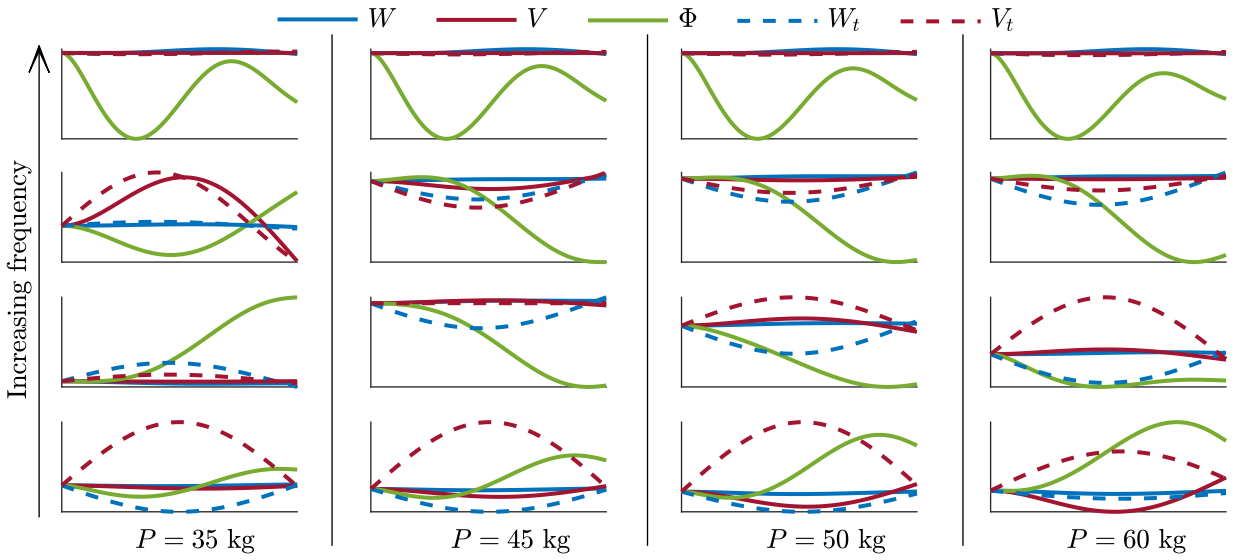

Figure 13: Theoretical mode shape variations during veering for the beam-tendon system with the tendon placed a general location. Corresponding mode shapes from the finite element model can be found in Fig. A.20.

3.4. Summary of the experimental validation

In this section, experimental validation of the proposed theoretical and numerical models has been presented. Overall, a good agreement between theoretical, numerical and experimental results has been observed, and all discrepancies can be attributed to the errors in the under-lying beam models. It was found that the beam-tendon system with an eccentrically placed tendon possesses two sets of vibration modes, i.e. beam-dominated and tendon-dominated modes. The natural frequencies of the beam-dominated modes depend not only on the magnitude of the applied tension, but also on the location of the tendon. It was observed that for the tendon placed in the centre of gravity, the beam-dominated natural frequencies decrease, while when the tendon is located at or after the shear centre, the natural frequencies of some of the beam-dominated modes increase. In addition, it was observed that the interaction and veering between the beam-dominated and tendon-dominated modes depends on the location of the tendon. Most notably, when the tendon is not placed on the axis of symmetry of the cross-section, bending-bending-torsion coupling is observed. The effect of the tendon location will be further studied both experimentally and computationally in section 4.

4. Further systematic studies

In the previous section, the experimental validation of the proposed theoretical model has been conducted. In this section, further systematic studies that explore the effect of the tendon location on free vibration and stability of the beam-tendon system are conducted.

4.1. Experimental results demonstrating the effect of tendon location

Here, the comparison of several sets of experimental data is given in order to show the effect of the tendon location. These data sets represent the frequency-loading diagrams for locations 1 to 4 in which the tendon is always placed on the axis of symmetry of the cross-section. The comparison can be seen in Fig. 14 in which the data measured in the z direction are used. It can be seen that all tendon-dominated modes coincide with each other very well. This indicates that the experiment was performed with sufficient accuracy and repeatability, and that the tendon-dominated modes are not influenced by the location of the tendon as expected.

The natural frequencies of the beam-dominated modes, on the other hand, exhibit very strong dependency on the location of the tendon as seen in Fig. 14 also summarised in Tab. 4. Each beam-dominated mode is

	location 1	location 2 (s.c.)	location 3 (c.g.)	location 4
1: 1F	-13.05	-14.14	-17.61	-28.37
2: 1L	19.07	3.3	3.24	-6.4
3: 1T	7.39	2.33	-5.32	-23.09
4: 2F	13.88	2.09	-9.33	-10.24
5: 2L	2.06	-3.48	-4.28	-7.14
6: 3F	4.93	-1.97	-11.07	-23.73
7: 4F	9.17	2.83	-4.7	-15.59
8: 2T	n/a	n/a	n/a	n/a
9: 3L	28.09	26.92	26.63	24.87
10: 5F	10.15	3.92	-4.27	-15.05

Table 4: The relative shifts (in %) of the experimental beam-dominated natural frequencies from Fig. 14 for the applied load equal to 90 kg with respect to the experimental natural frequencies of the under-lying beam.

influenced differently. The first mode always decreases with the applied axial load regardless of the tendon position. Other coupled flapping and torsional modes' natural frequencies decrease for the position of the tendon in the centre of gravity and further away from it (for positive e_y beyond the centre of gravity), and they increase when the tendon is placed in the shear centre and further away from it (for negative

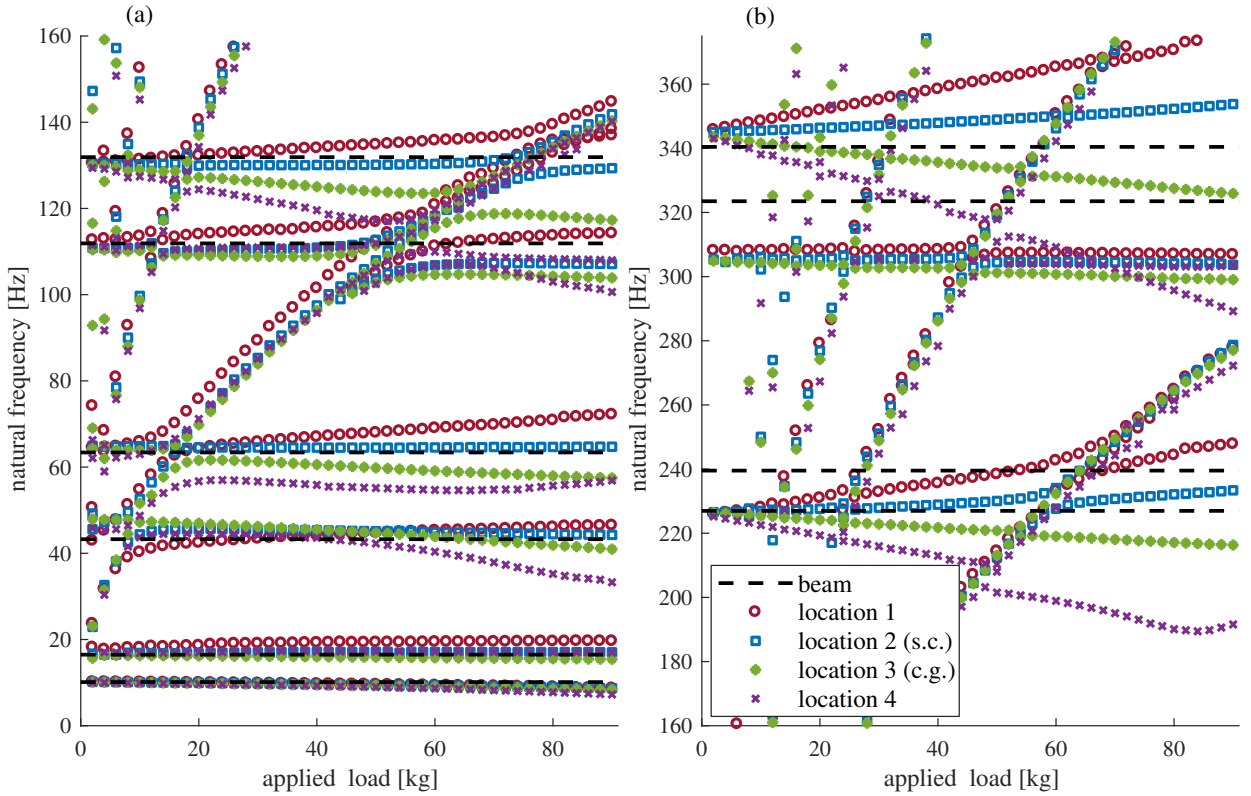

Figure 14: Comparison of experimental frequency-loading diagrams: (a) the frequency band between 0 Hz and 160 Hz, and (b) the continuation of (a) for the frequency band 160 Hz and 375 Hz. The black dashed lines indicates the experimental natural frequencies of the under-lying beam with the tip fixture.

y_0 beyond the shear centre). These findings are also supported by the numerical studies shown in the previous sections, and will be further emphasised in section 4.2 by further parametric studies. Since the beam-dominated frequency loci changes while the tendon-dominated ones stay the same, the veering regions are shifted accordingly, and as seen in the previous cases, their complexity varies due to coupling introduced by the tendon. The lead-lag bending modes were not properly excited in these data due to the placement of the shaker, but it will be shown that they are not influenced by changes in the y location of the tendon for the tendon is located on the sectional axis of symmetry.

It is worth noticing that the data obtained from the system with the tendon located in location 4 (furthest from the shear centre) exhibit some defects for the applied load higher than 70 kg. This can be seen in the 4^{th} mode, which suddenly increases without an apparent reason since no veering occurs. Similarly, the first mode in Fig. 14(b) (about 200 Hz) shows an unexpected increase in its frequency. These defects can be attributed to an imperfect clamped boundary conditions as will be further discussed in section 4.3.

4.2. The effect of the tendon location on the first three natural frequencies

The effect of the tendon location on the natural frequency of the first three vibration modes (first out-of-plane bending, first in-plane bending and first torsion) is studied in this section. The parametric studies were performed for three magnitudes of the applied forces, i.e. for $P = 200$, 400 and 600 N. The location of the tendon varied between $e_z \in [-h, h]$ and $e_y \in [2y_0, -y_0]$. The resulting variation in the natural frequencies can be seen in Fig. 15. The main observation is that the first lead-lag mode is not influenced as much as the other two. Even for the highest applied force, its natural frequency is shifted by approximately 0.5 % while the changes for the other two modes are about 20 %. The natural frequency of the first mode (1F) is highest when the tendon is placed in the shear centre and always lower for any other location. On the

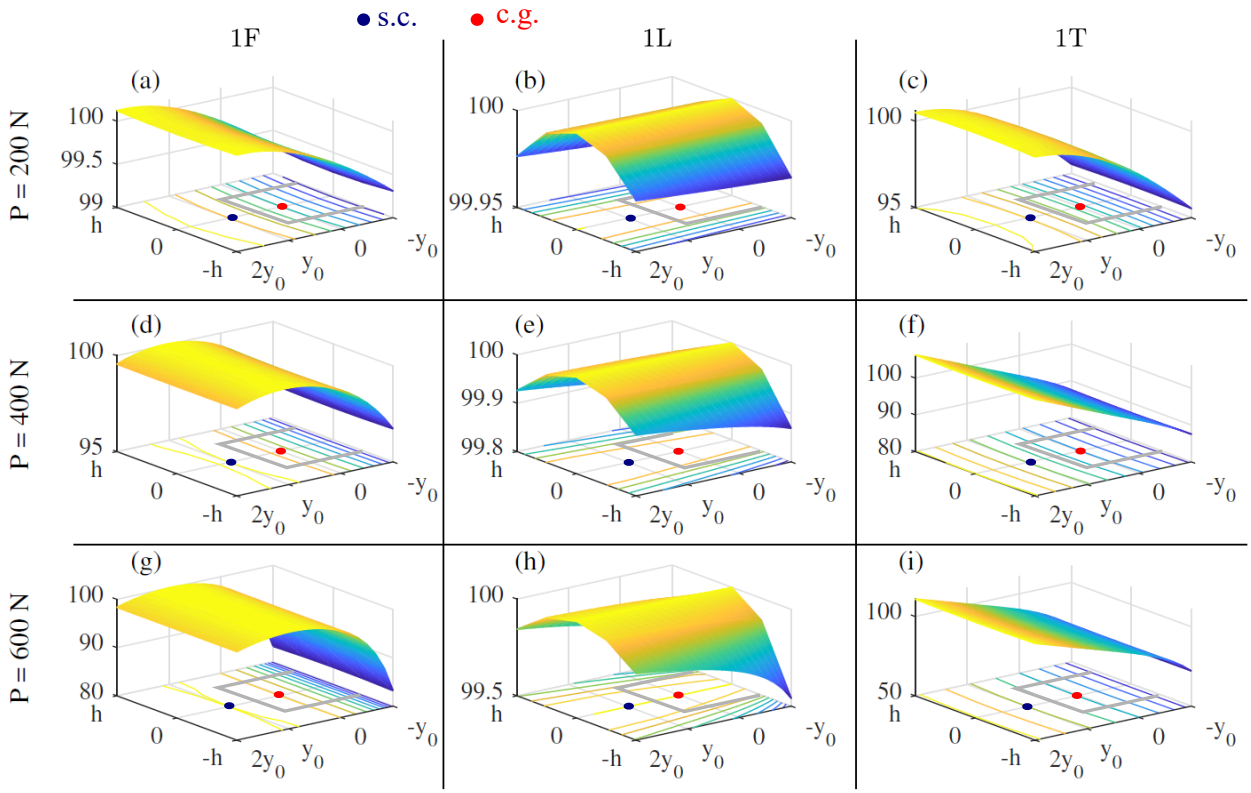

Figure 15: Parametric studies showing the effect of the tendon location on the first three vibration modes (1F, 1L and 1T). The surfaces are normalised so that the natural frequency of the beam-tendon system with the tendon placed in the shear centre is equal to 100 %. e_y varies between $-y_0$ and $2y_0$, and e_z between $-h$ and h.

other hand, the natural frequency of the first torsion mode is higher when the tendon is placed in $2y_0$. It can be also noticed that the flapping and torsion modes are mainly influenced by e_y while the lead-lag mode is influenced mainly by e_z. All these observation were also confirmed by the experimental data presented in section 4.1. In addition, it can be noticed that the natural frequency of the first lead-lag mode varies not only with e_z but also with e_y for $e_z \neq 0$. This is given by the fact that the general location of the tendon leads to the coupling between the two bending directions, and hence the natural frequencies are also influenced. The effect of e_z on the 1L is however small when compared to e_y.

4.3. The effect of the tendon location on structural stability of the beam-tendon system

Since the beam is axially loaded, its structural stability is investigated in this section. The critical force is obtained when the first natural frequency drops to zero. The mode shapes on which the system loses stability and the critical forces for different locations of the tendon are shown in Fig. 16. The critical force is at its maximum when the tendon is placed in the shear centre, and the stability is lost by pure bending (no torsion is observed). This is in line with classical stability studies [8, 9] where it was shown that the critical force in case of bending-torsion is always lower than for pure bending. When the tendon is placed in $e_y = 2y_0$ the critical force is lower and the stability is lost by bending-torsion of the beam. When the tendon is placed in the sectional centre of gravity, the critical force is lower than for the placement in the shear centre, and the mode shape shows bending-torsion coupling. For the placement in $e_y = -y_0$, the lowest critical force is observed. This critical force correspond to 74.6 kg which means that the beam-tendon system should have lost its stability during the experimental investigation for the tendon in location 4. However, as seen from the results in Fig. 14 this did not happened. It is believed that this is caused by the flexibility of the clamp combined with the additional stiffness provided by the shaker. During the eccentric loading, the

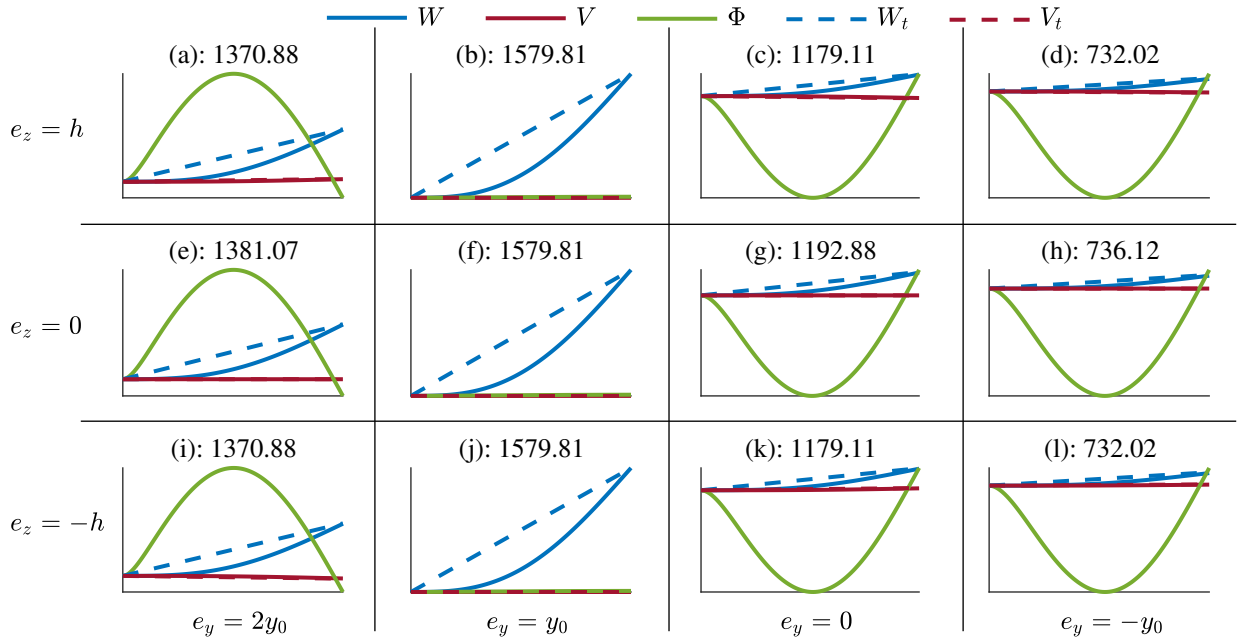

Figure 16: Stability of the beam-tendon system for different locations of the tendon. The numbers in the plot titles represent the critical forces in Newton. The equivalent set of the mode shapes as obtained from the finite element model can be seen in Fig. A.21.

beam is significantly bent so it is possible that it slides in the clamp and therefore the considered boundary conditions (i.e. the ideal fixed end) does not accurately represent the experimental set-up for such a high eccentrically applied load. As mentioned in section 4.1, some defects in the experimental data were observed when the loading exceeded 70 kg. It is possible that these effects are also caused by the finite flexibility of the clamp.

While no effect of e_z is observed when tendon is placed in, under and above the shear centre, the effect of e_z is seen for other cases. The offset of the tendon from the axis of symmetry lowers the critical force (and changes the mode shapes), but the decrease is not significant. The critical force does not depend on the sign of e_z.

The finite element model was also used to find the critical force which corresponds to the zero natural frequency of the first mode. This was only possible for the cases where $e_z = 0$, because for the tendon placed off the axis of symmetry, the bending of the beam which is caused by the static axial force was so large that the first step (static analysis) in the finite element calculation did not converge. For $e_z = 0$, the critical force obtained from the FE model were equal to 1329.2 N for $e_y = 2y_0$, 1485.2 N for $e_y = y_0$, 1179.8 N for $e_y = 0$ and 782.8 N for $e_y = -y_0$. These critical forces are comparable to the theoretical ones, validating the theoretical model proposed beyond the loading range that could be achieved in the experiment.

5. Discussion

In this paper, the theoretical model of the beam axially loaded by an eccentrically placed tendon has been proposed and its experimental validation in terms of the frequency-loading diagrams conducted. In this section, the main findings, assumptions and limitations, and a possible application of the beam-tendon system are discussed.

The validation of the theoretical model was conducted using the bench-top experiment and a high-fidelity finite element model. The validation was performed on the thin-walled beam with a mono-symmetric open cross-section which was loaded in several locations by a tendon. Throughout the paper, a good agreement between the theoretical, experimental and numerical results has been observed. As in the previous

studies [21, 24], it was observed that two sets of vibration modes - beam-dominated and tendon-dominated ones - are present in the beam-tendon system, and that they interact with each other through frequency loci veering. Unlike in the previous studies, however, the effect of the tendon location was investigated in the detail and it was observed that (i) it has a significant effect on the natural frequencies of the beam-dominated modes while it does not influence the tendon-dominated ones, (ii) the natural frequency of the first system mode decreases regardless of the location of the tendon, while the natural frequencies of other modes can increase or decrease depending on the tendon's location and (iii) the location of the tendon has a significant effect on the structural stability and the critical force reaches its maximum when the tendon is placed in the shear centre.

A number of assumptions have been considered to derive the governing equations of motion as documented in [8, 9, 15] in detail. Most importantly, the Euler-Bernoulli theory with warping was used and the tendon was modelled as a taut string where it was assumed that its diameter remains constant [6]. In order to satisfy the Euler-Bernoulli theory, the transverse shear deformation and rotary inertia effects were neglected [3]. In addition, the effect of the static axial load, which bends the beam for eccentric placement, was neglected in the theoretical model. These assumptions do not seem to limit the accuracy of the frequency-loading diagrams. The derived model is linear and the linear modal analysis has been used since no apparent non-linearity was observed in the system or experimental set-up.

The structural damping or other energy dissipation effects have not been included in the proposed theoretical or numerical models. This is justified by the fact that the damping in the present system is very weak and hence it has a negligible impact on the natural frequencies and mode shapes. However, in general, if the damping is shown to be significant, it could be included in the theoretical model using, for example, Kelvin-Voigt model of damping [36]. Moreover, when the tendons are designed to specifically introduce very high or non-linear damping into a vibrating system (for example, the use of the smart memory alloy cables to introduce passive structural damping was investigated in [37] or semi-active friction tendons were considered in [38]), an appropriate damping model must be employed.

The motivation of the research was the application of an active blade-tendon system in rotorcraft as suggested in [22, 25] where it was shown that the blade-tendon system with the tendon placed in the elastic axis can be used as a means of resonance avoidance [26, 28]. The active tendon concept should ultimately introduce control capabilities by which the natural frequencies of rotorcraft blade could be adjusted and, in turn, this should enable rotorcraft to operate over a wider range of rotor configurations or rotor speeds, thereby increasing their efficiency and decreasing their fuel burn, air pollution and noise emission in the future. As seen in this paper, the sectional location of the tendon can significantly influence the modal properties of the under-lying beam as well as its stability. Therefore, the future development of the active tendon concept should take this into account and examine the possibility that the resonance avoidance can be achieved not only by the applied force, but also by adjusting the position of the tendon within the cross-section.

6. Conclusions

In this paper, the beam-tendon system with an eccentrically placed tendon was studied for the first time. A theoretical model of the system was proposed and thoroughly validated using experimental and numerical studies. The effect of the tendon location was examined in detail and the main findings can be summarised as follows:

- The location of the tendon has significant impact on the beam-dominated modes, while the tendon-dominated modes remain the same.
- Due to the additional coupling introduced by an eccentrically located tendon, veering between the beam-dominated and tendon-dominated modes is complex and bending-bending-torsion coupling is observed.
- Each natural frequency is affected differently by the tendon's location. For the investigated system, it can be concluded that (i) the natural frequency of the first mode always decreases regardless of the

tendon's location, (ii) the natural frequencies of other flapping and torsional modes increase when the tendon is placed in the shear centre and further away for the centre of gravity, and decrease when the tendon is placed in the centre of gravity and further away from the shear centre, and (iii) the lead-lag modes are influenced when the tendon is not placed on the axis of symmetry, in which case various locations along the axis of symmetry affect their natural frequencies as well as the natural frequencies of other modes due to the bending-bending-torsion coupling introduced.

- The sectional location of the tendon has significant impact on the stability of the system. The critical force is at its maximum when the tendon is placed in the shear centre and the stability is lost due to pure bending of the beam in this case. The critical force decreases with the distance from the shear centre and the loss of stability due to bending-torsion is observed.

Acknowledgements

The authors would like to acknowledge the financial support of the European Community's Horizon 2020 Program provided through the project "Shape Adaptive Blades for Rotorcraft Efficiency (SABRE)", Grant Agreement 723491.

References

[1] S. Korkmaz, A review of active structural control: challenges for engineering informatics, Computers and Structures 89 (23-24) (2011) 2113–2132. doi:10.1016/j.compstruc.2011.07.010.
[2] A. Preumont, Vibration Control of Active Structures: An Introduction, Springer Netherlands, 2012.
[3] S. S. Rao, Vibration of Continuous Systems, 2007.
[4] A. Rosen, Structural and dynamic behaviour of pretwisted rods and beams, Applied Mechanics Reviews 44 (12) (1991) 483–515.
[5] D. Hodges, Nonlinear Composite Beam Theory, American Institute of Aeronautics and Astronautics, 2006.
[6] A. H. Nayfeh, P. F. Pai, Linear and Nonlinear Structural Mechanics, Wiley, 2008.
[7] L. Virgin, Vibration of Axially-Loaded Structures, Cambridge University Press, 2007.
[8] Z. Bazant, L. Cedolin, Stability of Structures: Elastic, Inelastic, Fracture and Damage Theories, World Scientific, 2010.
[9] S. Timoshenko, J. Gere, Theory of Elastic Stability, Engineering societies monographs, Dover Publications, 1961.
[10] J. Banerjee, S. A. Fisher, Coupled bending-torsional dynamic stiffness matrix for for axially loaded beam elements, International Journal for Numerical Methods in Engineering 33 (1992) 739–751. doi:10.1016/0020-7683(94)90075-2.
[11] A. Leung, Natural shape functions of a compressed Vlasov element, Thin-Walled Structures 11 (5) (1991) 431–438. doi:10.1016/0263-8231(91)90037-J.
[12] P. O. Friberg, Beam element matrices derived from Vlasov's theory of open thinwalled elastic beams, International Journal for Numerical Methods in Engineering 21 (7) (1985) 1205–1228. doi:10.1002/nme.1620210704.
[13] L. Jun, L. Wanyou, S. Rongying, H. Hongxing, Coupled bending and torsional vibration of nonsymmetrical axially loaded thin-walled Bernoulli-Euler beams, Mechanics Research Communications 31 (6) (2004) 697–711. doi:10.1016/j.mechrescom.2004.04.005.
[14] A. Prokić, R. Mandić, M. Vojnić-Purčar, Influence of bimoment on the torsional and flexural-torsional elastic stability of thin-walled beams, Thin-Walled Structures 89 (2015) 25–30. doi:10.1016/j.tws.2014.12.005.
[15] V. Z. Vlasov, Thin-Walled Elastic Beams, Israel Program for Scientific Translations Ltd, 1961.
[16] D. B. Holland, I. Stanciulescu, L. N. Virgin, R. H. Plaut, Vibration and large deflection of cantilevered elastica compressed by angled cable, AIAA Journal 44 (7) (2006) 1468–1476. doi:10.2514/1.18000.
[17] S. Nudehi, R. Mukherjee, S. Shaw, Active vibration control of a flexible beam using a buckling-type end force, Journal of Dynamic Systems, Measurement, and Control 128 (2) (2006) 278. doi:10.1115/1.2192836.
[18] J. Issa, R. Mukherjee, S. Shaw, Vibration suppression in structures using cable actuators, Journal of Vibration and Acoustics 132 (3) (2010) 031006. doi:10.1115/1.4000783.
[19] G. Skidmore, W. Hallauer, Modal-space active damping of a beam-cable structure: theory and experiment, Journal of Sound and Vibration 101 (2) (1985) 149 – 160. doi:10.1016/S0022-460X(85)81211-6.
[20] R. Dibble, B. Titurus, Helicopter rotor blade modal tuning using internal preloads, in: International Seminar on Modal analysis (ISMA), 2016.
[21] V. Ondra, B. Titurus, Theoretical and experimental modal analysis of a beam-tendon system, Mechanical Systems and Signal Processing 132 (2019) 55 – 71. doi:10.1016/j.ymssp.2019.06.016.
[22] V. Ondra, B. Titurus, Free vibration analysis of rotating pre-twisted beams subjected to tendon-induced axial loading, Journal of Sound and vibration, under review, 2019.
[23] V. Ondra, B. Titurus, Numerical and experimental modal analysis of a cantilever beam axially loaded by a tendon which is attached in a single spanwise location, in: M. L. Mains, B. J. Dilworth (Eds.), Topics in Modal Analysis & Testing, Volume 8, Springer International Publishing, Cham, 2020, pp. 107–116. doi:10.1007/978-3-030-12684-1_10.

[24] V. Ondra, B. Titurus, Free vibration and stability analysis of a cantilever beam axially loaded by an intermittently attached tendon, Journal of Vibration and Control, under review, 2019.
[25] J. Rauleder, B. G. van der Wall, A. Abdelmoula, D. Komp, S. Kumar, V. Ondra, B. Titurus, B. K. S. Woods, Aerodynamic Performance of Morphing Blades and Rotor Systems, in: AHS International 74th Annual Forum & Technology Display, Phoenix, Arizona, USA, 2018.
[26] V. Ondra, R. P. Dibble, B. Titurus, B. K. S. Woods, An active tendon concept in rotorcraft with variable speed rotors: free vibration perspective, in: AIAA Scitech 2019, no. January, 2019, pp. 1–14. doi:10.2514/6.2019-0857.
[27] V. Ondra, R. Dibble, B. Titurus, Towards an application of an active tendon in rotorcraft: A numerical and experimental study of coupled bending-torsion vibration of a beam-tendon system, in: 28th International Conference on Noise and Vibration engineering (ISMA 2018), 2018, pp. 3645–3659.
[28] R. Dibble, V. Ondra, B. Titurus, Resonance avoidance for variable speed rotor blades using an applied compressive load, Aerospace Science and Technology 88 (2019) 222 – 232. doi:10.1016/j.ast.2019.03.009.
[29] R. P. Dibble, V. Ondra, B. K. S. Woods, B. Titurus, Aeroelastic eigenvalue analysis of a variable speed rotor blade with an applied compressive load, in: AIAA Scitech 2019, no. January, 2019, pp. 1–17. doi:10.2514/6.2019-1355.
[30] J. Kierzenka, L. Shampine, A BVP solver based on residual control and the Matlab PSE, ACM Transactions on Mathematical Software 27 (3) (2001) 299–316. doi:10.1145/502800.502801.
[31] Abaqus 6.14 Online Documentation (2014).
[32] J. Bendat, A. Piersol, Random Data: Analysis and Measurement Procedures, John Wiley & Sons, Inc., 2000.
[33] B. Peeters, H. Van Der Auweraer, P. Guillaume, J. Leuridan, The PolyMAX frequency-domain method: a new standard for modal parameter estimation?, Shock and Vibration 11 (2004) 395–409. doi:10.1155/2004/523692.
[34] N. C. Perkins, C. D. Mote, Comments on curve veering in eigenvalue problems, Journal of Sound and Vibration 106 (3) (1986) 451–463. doi:10.1016/0022-460X(86)90191-4.
[35] B. R. Mace, E. Manconi, Wave motion and dispersion phenomena: Veering, locking and strong coupling effects, The Journal of the Acoustical Society of America 131 (2) (2012) 1015–1028. doi:10.1121/1.3672647.
[36] B. Geist, J. R. McLaughlin, The effect of structural damping on nodes for the Euler-Bernoulli beam: a specific case study, Applied Mathematics Letters 7 (3) (1994) 51–55. doi:10.1016/0893-9659(94)90112-0.
[37] P. Thomson, G. Balas, P. Leo, The use of shape memory alloys for passive structural damping, Smart Materials and Structures 4 (1) (1995) 36.
[38] H. Garrido, O. Curadelli, D. Ambrosini, Experimental and theoretical study of semi-active friction tendons, Mechatronics 39 (2016) 63–76. doi:10.1016/j.mechatronics.2016.08.005.

Appendix A. Mode shapes obtained from the finite element model

In this appendix, the mode shapes obtained from the finite element model are presented. They complement the mode shapes computed from the theoretical model and extracted experimental mode shapes that are shown in the main body of the paper.

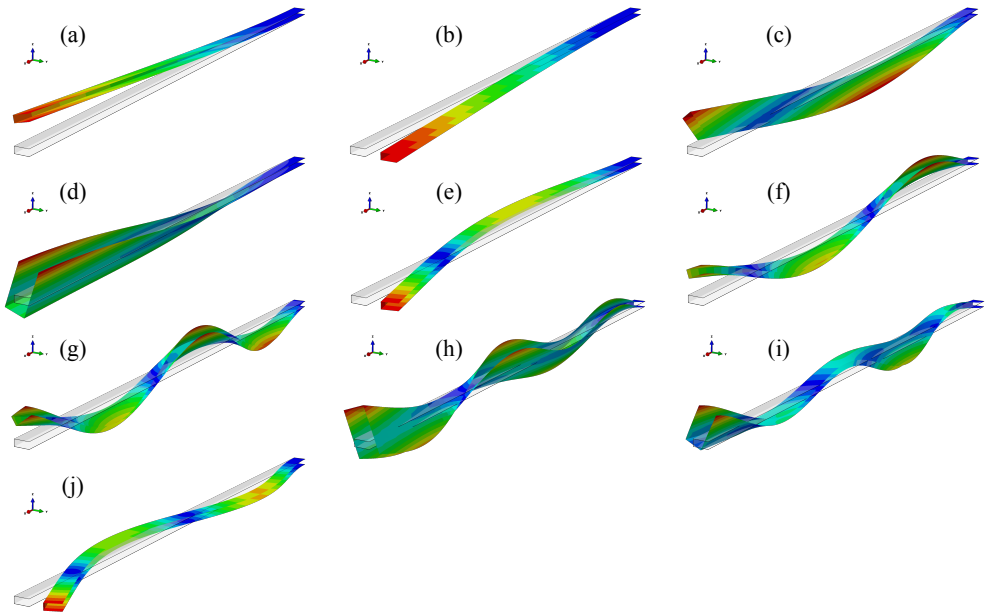

Figure A.17: The mode shapes of the beam without the tip fixture as obtained by the finite element model. Equivalent set of mode shapes can be seen in Fig. 6.

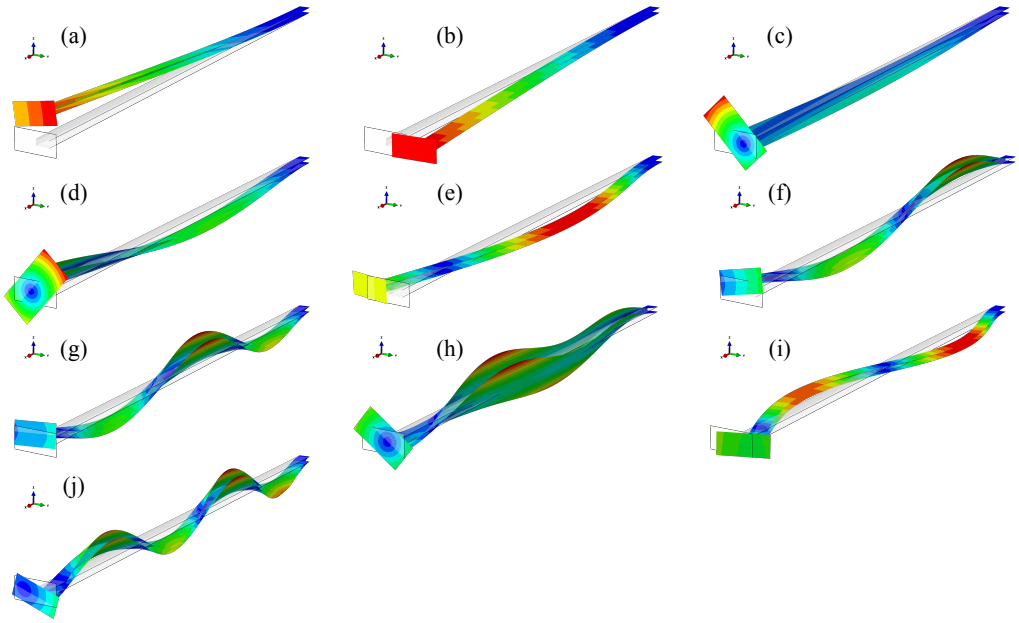

Figure A.18: The mode shapes of the beam with the tip fixture as obtained by the finite element model. The equivalent set of the theoretical mode shapes can be seen in Fig. 8.

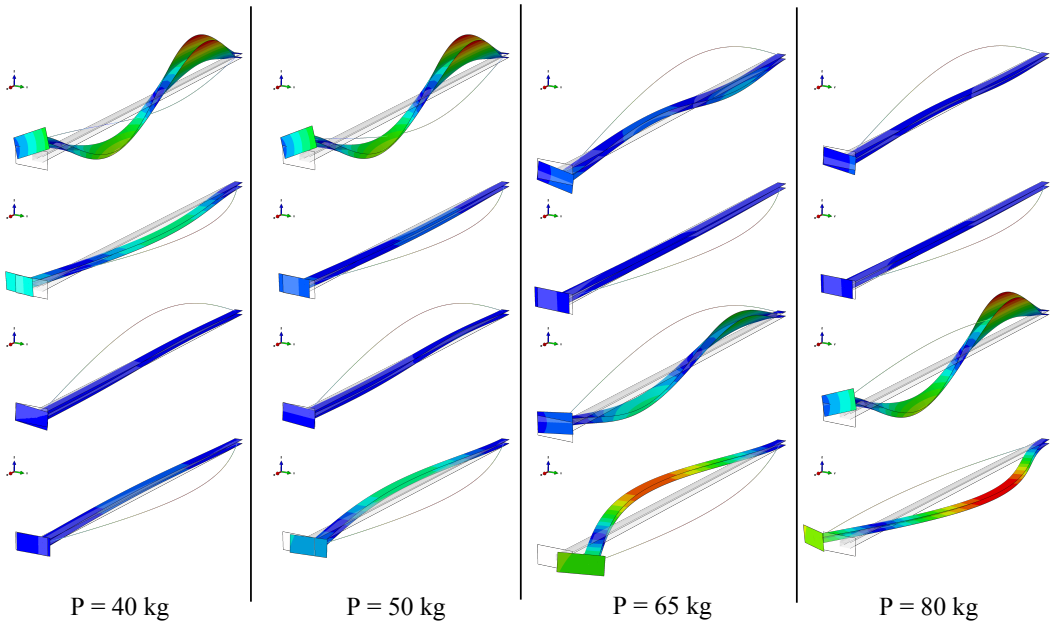

Figure A.19: Numerical mode shapes variations during veering for the beam-tendon system with the tendon placed in the centre of gravity. The equivalent set of the theoretical mode shapes can be seen in Fig. 11.

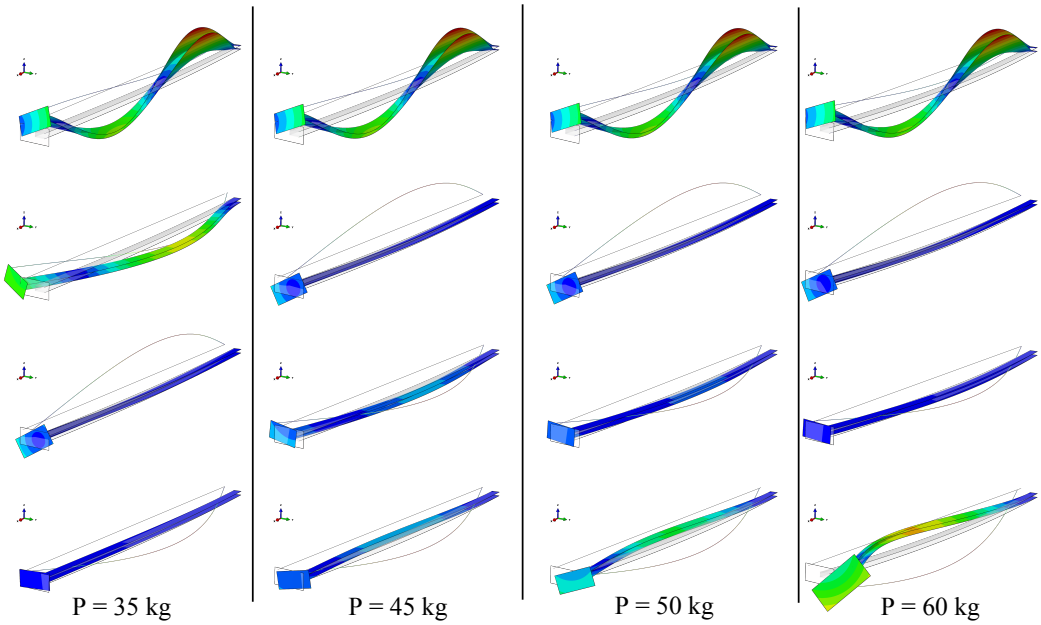

Figure A.20: Numerical mode shapes variations during veering for the beam-tendon system with the tendon placed in a general location. The equivalent set of the theoretical mode shapes can be seen in Fig. 13.

(a): 1328.2 (b): 1485.2 (c): 1197.8 (d): 782.3

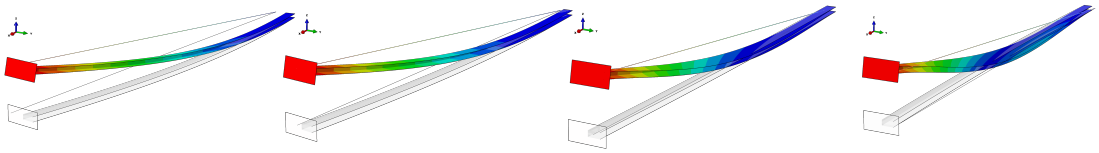

Figure A.21: Stability of the beam-tendon system for different locations of the tendon. The numbers in the plot titles represent the critical forces in Newton. Equivalent set of mode shapes can be seen in Fig. 16.